

Fault characterization and flow barrier detection using capacitance-resistance model and diagnostic plots

Oscar I.O. Ogali^a, Oyinkepreye D. Orodu^{b,*}

^a Department of Petroleum and Gas Engineering, University of Port Harcourt, Port Harcourt, Rivers State, Nigeria

^b Department of Petroleum Engineering, Covenant University, Ota, Ogun State, Nigeria

ARTICLE INFO

Keywords:

Capacitance-resistance model
Dynamic flow capacity plots
Flow storage index
Interwell communication
Fault characterization
Waterflooding

ABSTRACT

Advantageous for its speed and far less data requirements, the Capacitance-Resistance Model has been successfully applied to waterflood performance prediction and optimization, gas flood optimization and reservoir characterization. In this study, a diagnostic plot and an iterative workflow that incorporates geological and well data with calibrated CRM results, were developed for depicting injector-producer communication, thereby characterizing a reservoir of interest. These were validated using three synfield cases. Thereafter, two selected faults in a Far East Oil Field (FEOF) were characterized and sealing baffles identified around these faults. Based on the results, one fault had several sections with varying degrees of communication and sealing baffles on either side of the fault. The second fault was mostly sealing with no sealing baffles on either side. The new diagnostic plot and workflow also quality-checked interwell connectivities from calibrated CRM, thereby substantially improving the fault characterization process. With far fewer and readily available data from oilfields, reduced physics models like CRM and the Diagnostic Plots are tools for cost-effective and speedy reservoir characterization, and to corroborate results of Interference and Tracer Tests, as well as 4D Seismic.

1. Introduction

Ample characterization of a reservoir using all available data, is paramount in several processes in oil and gas operations, such as selection of optimal development strategies in each development stage, as well as predicting future performance of the reservoir (Ertekin et al., 2001; Sayyafzadeh et al., 2011; Yousefi et al., 2019). The conventional approach to reservoir characterization is tedious, computationally expensive and time-consuming, involving complicated geophysical, geological, petrophysical and PVT data, as well as the selection of “representative” geological models, reservoir simulations and history-matching (Cao et al., 2014; Kaviani et al., 2012; Mamghaderi and Pourafshary, 2013).

Reservoir properties between wells can be inferred and/or quantified via interwell communication (Kaviani et al., 2012; Ogali and Orodu, 2020). Flooding schemes have historically been used to understand interwell communication and identify flow barriers and high-permeability flow paths between wells (Izgec and Kabir, 2012; Yousefi et al., 2019). Streamline simulations have been used to obtain well allocation factors, quantify interwell connectivities and consequently, characterize reservoirs (Batycky et al., 2008; Thiele et al., 2010;

Thiele and Batycky, 2003). However, they are also time-consuming, computationally expensive, and sensitive to some data sets (Sayyafzadeh et al., 2011).

Identifying faults and flow barriers in the reservoir of interest and adequately quantifying the transmissibilities across these barriers and their extents enable proper evaluation of fluid flow directions within the reservoir. Thus, they are crucial in reservoir characterization (Mohammady et al., 2018; Pouladi et al., 2018). Faults are typically sealing or non-sealing. Sealing faults completely stop lateral flow, while non-sealing (or leaky) faults reduce the cross-fault rate of flow. This is because, the transmissibilities across non-sealing faults are typically less than undisturbed permeable strata (Ogali and Orodu, 2020; Pouladi et al., 2018; Yaxley, 1987).

The throw of non-sealing faults tends to be insufficient to cause complete separation of permeable strata (Pouladi et al., 2018; Yaxley, 1987). However, the “sealability” of a fault cannot be adequately assessed using fault throw (Zhang et al., 2011). Although fault characteristics are commonly presented as similar over the fault plane, the transmissibility of a fault can be highly heterogeneous and influenced by many factors (Moretti, 1998; Zhang et al., 2011). The sealing or non-sealing nature of a fault depends on the time scale and may evolve

* Corresponding author.

E-mail address: oyinkepreye.orodu@covenantuniversity.edu.ng (O.D. Orodu).

<https://doi.org/10.1016/j.petrol.2021.109817>

Received 2 July 2021; Received in revised form 2 November 2021; Accepted 7 November 2021

Available online 11 November 2021

0920-4105/© 2021 Elsevier B.V. All rights reserved.

over time (Aubert et al., 2021; Biryukov and Kuchuk, 2012; Moretti, 1998; Yaxley, 1987), due to possible seismic activities (Keranen et al., 2013), or injection pressurization and induced seismicity (Mosaheb and Zeidouni, 2018; Rutqvist et al., 2007).

Besides geological and geophysical based methods of identifying and evaluating faults (Takam Takougang et al., 2019; Wu and Hale, 2016; Zhang et al., 2011), pressure transient tests have also been used extensively for identifying and characterizing faults, based on their sealing ability and physical characteristics (such as distance to the well of interest, dip angle). The sealing ability attempts to quantify the fluid or pressure flow across the fault (Hosseini, 2019; Yaxley, 1987). However, the simplifying assumptions of this approach make it somewhat unsuitable for reservoirs with complex fault configurations (Liu et al., 2018; Pouladi et al., 2018). Other alternatives like numerical well testing and the Fast Marching Method (FMM) proposed by Pouladi et al. (2018) have limitations in terms of computational costs and their reliance on bottomhole pressure (BHP) data which may be unavailable in legacy oilfields. However, these approaches rely on BHP data for accuracy, making them less likely to apply to legacy oilfields.

Historical rate (injection and production) data are typically abundant in all fields including marginally economic fields, and contain information about well and reservoir behaviour (Albertoni and Lake, 2003; Jansen and Kelkar, 1997; Ogali and Orodu, 2020; Soroush et al., 2014). Inferences on interwell connectivities are typically obtained from flooding schemes (Izgec and Kabir, 2012; Kaviani and Valkó, 2010). This is because, they depend on well distances, heterogeneities (or reservoir characteristics) between wells and reservoir geometry (Yousefi et al., 2019).

Several studies investigated using readily available historical data to quantify connectivities between wells and consequently, optimize recovery from petroleum reservoirs. Malik et al. (1993) developed an approach based on hydraulic interwell connectivity concept to characterize interwell connectivities using historical rate data and static geological data. Jansen and Kelkar (1997) decomposed historical production data using Wavelet Transformation, to evaluate interwell relationships. Using Spearman rank correlations and historical rate data, Heffer et al. (1997) evaluated communications between injector-producer well pairs, and associated these well-pair interactions with geomechanics. Panda and Chopra (1998) applied artificial neural networks (ANN) to historical rate data and several other data sets to estimate injector-producer interactions in a heterogeneous-permeability field, thereby identifying permeability trends and flow barriers.

Soerawinata and Kelkar (1999) evaluated injector-producer interactions, as well as possible interferences (constructive and destructive interferences) between injectors and producers, using a statistical approach and superposition principle. Using weight factors and diffusivity filters, Albertoni and Lake (2003) applied constrained multivariate linear regression (MLR) to quantify injector-producer connectivities. The diffusivity filters, which depend on static reservoir properties, account for time lags between injector-producer well pairs. In 2005, Yousef et al. presented the Capacitance-Resistance Model (CRM), a reduced physics approach to quantifying interwell interactions and predicting reservoir performance. Besides quantifying interwell connectivities, two other advantages of the CRM are its far less data requirements and speed (de Holanda et al., 2018; Sayarpour et al., 2009). Dinh and Tiab (2008) estimated injector-producer connectivities using the constrained MLR approach proposed by Albertoni and Lake (2003) and BHP data but, excluded diffusivity filters.

Other approaches that utilize production dynamic data have also been implemented to estimate interwell interactions. Liu et al. (2009) forecasted injector-producer relationships by applying the extended Kalman filter to historical rate data. Kaviani and Valkó (2010) presented the multiwell productivity index to estimate interwell connectivity in a homogeneous synfield under several operating conditions. Quantifying interwell interactions based on historical rate data have been achieved using Finite Impulse Response (FIR) curves (Lee et al., 2009) and

multivariate autoregressive model with exogenous inputs (M-ARX) (Lee et al., 2010).

Based on adequacy of interwell connectivity estimates, Shahvali et al. (2012) compared CRM and streamline simulation; Artun (2016) compared CRM and artificial neural networks. Gherabati et al. (2017) presented a reservoir network model for quantifying interwell formation characteristics using historical data, bottomhole pressure (BHP) data, along with well and reservoir boundary locations. Arunthavanathan et al. (2021) applied a hybrid deep learning approach to successfully detect and diagnose faults in a process system. This showcases the application of domain knowledge transferrable to other disciplines and as utilized in the hybrid networks by Wang et al. (2021) and Yu et al. (2021).

Using an interpretable recurrent graph neural network (GNN) as well as historical rate and BHP data, Wang et al. (2021) developed a model that simulates the energy exchange or “real interwell flow regularity” between wells, while incorporating the time-lag and attenuation phenomena. Yu et al. (2021) applied two-layer neural networks with a sparsity-promoting regularization function for interwell connectivity pattern estimation based on the weight of the network. They stated that the application of the regularization approach is hinged on reservoir engineering domain expertise.

However, physics-based approaches to interwell connectivity pattern recognition and estimation removes the black-box nature of neural networks, and can incorporate the application of diagnostic plots analogue to reservoir heterogeneity estimation plots like the Lorenz plot, and coefficients such as Koval factor, Gelhar-Axness, and Dykstra-Parsons. Another limitation of these neural network approaches is their strong reliance on BHP data for accuracy. Typically, BHP data are not available for legacy oilfields. Unlike these approaches, CRM has been tested for syn-reservoirs and field case studies without BHP data, with acceptable results. It is a simplistic, yet robust approach that incorporates statistical regression analysis, thereby avoiding the rigor, time and data consumption process of machine learning approaches, as well as reservoir numerical simulation that also requires detailed geological models as a backbone. The CRM was therefore used in this study to identify and characterize faults and flow barriers.

2. Capacitance resistance model

Based on total fluid mass balance and linear productivity index, Yousef et al. (2005) introduced the capacitance-resistance model (CRM), a reduced physics approach that quantifies interwell connectivities using historical rate data and bottomhole pressure data if available. The CRM is a semi-analytical solution to an ordinary differential equation resulting from the combination of an advanced time-dependent Material Balance Equation and the Productivity Model (Soroush et al., 2014; Yousefi et al., 2019). It therefore yields an approximate representation of the dynamics of the system, using smaller set of fitting parameters (Moreno, 2013). These parameters are principally connectivity indices and time constants, which are “tuned” using historical rate (and possibly BHP) data (Kaviani et al., 2012; Sayarpour et al., 2009). The basic CRM is presented in Equation (1) (Yousef et al., 2005).

$$\frac{dq}{dt} + \left\{ \frac{1}{\tau} \bullet q(t) \right\} = \left\{ \frac{1}{\tau} \bullet w(t) \right\} - \left\{ J \bullet \frac{dP_{wf}}{dt} \right\} \quad (1)$$

Where: $q(t)$ = production rate; $w(t)$ = injection rate; P_{wf} = producer bottomhole flowing pressure (or BHP of producer); J = producer productivity index; τ = time constant = $\frac{c_t \bullet V_p}{J}$; c_t = total compressibility; V_p = pore volume.

Some of the main assumptions in deriving the CRM differential equation are: (i.) slightly compressible fluids and pore volume; (ii.) immiscible fluids (or phases) coexist with negligible capillary pressure; (iii.) instantaneous equilibrium within the control volume; and (iv.) temperature and productivity index are constant (Liang et al., 2007;

Sayarpour et al., 2009). Consequently, the “initial” CRM could not accommodate: (a.) changes in number of active producers (introduction of new wells and/or shutting in wells for extended periods); (b.) large variations in fluid compressibility as seen in systems involving gas; (c.) well workovers, which substantially alter productivity indices of such wells; and (d.) presence of aquifer support (Altaheini et al., 2016).

Based on three different control volumes (entire field volume, producer drainage volume, and injector-producer drainage volume) and using superposition in time, Sayarpour et al. (2009) developed analytical solutions to the fundamental differential equation of CRM. The resulting CRMs are: (i.) CRM of a Tank (CRMT); (ii.) CRM of a Producer (CRMP); and (iii.) CRM of an Injector-Producer well-pair (CRMIP) respectively. By including injector-producer connectivity index to the CRMT proposed by Sayarpour et al. (2009), Chen et al. (2010) enabled the evaluation of the flow at the outer boundaries of a field of interest.

The segmented CRM and compensated CRM were presented by Kaviani et al. (2012) to accommodate common field conditions, such as variations in number of active producers (due to additional producers or relatively-long shut-in periods of existing producers), and unavailability of BHP data accompanied by large BHP changes. Combining the CRM with a simple dynamic model, Moreno (2013) developed a multilayer CRM that accounted for variations in connectivities with time. Soroush et al. (2014) presented the Multi-well Compensated Capacitance Model (MCCM), a modification of the compensated CRM that accommodates variations in number of producers and skin factor of producers.

Altaheini et al. (2016) presented the CRMID, which combines the natural depletion of CRMP and the characterization ability of CRMIP. They also presented several workflows that improve the versatility of CRM. In order to reduce the CRM’s dependency on history matching length, Lesan et al. (2018) developed the dynamic CRM (DCRM), which considers dynamic time constants. Using gas density and average reservoir pressure, Yousefi et al. (2019) extended the application of CRM to compressible flow (immiscible gas flooding).

The CRM has been coupled with other models to improve its versatility, such as: (i.) fractional flow models (Gentil’s and Koval’s) (Liang et al., 2007; Sayarpour et al., 2009; Weber et al., 2009); (ii.) aquifer models (Izgec, 2012; Izgec and Kabir, 2010, 2012); (iii.) decline curve analysis (Salazar et al., 2012); (iv.) production logging tool data and fractional flow model (Mamghaderi and Pourafshary, 2013); (v.) two-phase model and fractional flow model (Cao et al., 2014); (vi.) heuristic methods and fractional flow model (Eshraghi et al., 2016); and (vii.) ensemble fractional flow model (Oliveira et al., 2021).

There have been diverse applications of CRM, such as waterflood management and optimization (Izgec, 2012; Liang et al., 2007; Mamghaderi and Pourafshary, 2013; Moreno, 2013; Oliveira et al., 2021; Sayarpour et al., 2009; Weber et al., 2009); primary recovery (Nguyen et al., 2011; Soroush and Rasaei, 2018), aquifer assessment and prediction (Izgec and Kabir, 2010, 2012; Izgec, 2012), performance prediction and optimization of gas flooding (Eshraghi et al., 2016; Laochamroonvorapongse et al., 2014; Yousefi et al., 2019) and reservoir characterization (Delshad et al., 2009; Jafroodi and Zhang, 2011; Mohamdally et al., 2018; Ogali and Orodu, 2020; Yousefi et al., 2006). As de Holanda et al. (2018) aptly put it, CRM can be used to confirm the presence of faults (leaky or sealing), and high-permeability flow paths, evaluate reservoir compartmentalization and inter-reservoir communication, and optimize allocation of injection fluid to injectors during improved oil recovery.

Based on linear variation in injection rate (LVIR) and step variation in BHP (SVBHP), and possible interactions between a given producer and several injectors in a waterflood, the CRM used is presented in Equation (2).

$$\hat{q}_j(t_n) = \frac{\text{Production}}{\text{Term}} + \frac{\text{Injection}}{\text{Term}} + \frac{\text{BHP}}{\text{Term}} \quad (2)$$

Where:

$$\begin{aligned} \text{Production Term} &= q_j(t_0) \cdot e^{-\left(\frac{t_n-t_0}{\tau_j}\right)} \\ \text{Injection Term} &= \sum_{i=1}^I \left\{ \lambda_{ij} \cdot \sum_{m=1}^n \left[\left(e^{-\frac{t_n-t_m}{\tau_{ij}}} - e^{-\frac{t_n-1-t_m}{\tau_{ij}}} \right) \cdot w_i(t_m) \right] \right\} \\ \text{BHP Term} &= \sum_{k=1}^K \left\{ \nu_{kj} \cdot \left[\left(P_{wf_j}(t_0) \cdot e^{-\left(\frac{t_n-t_0}{\tau_{kj}}\right)} - (P_{wf_k}(t_n)) + \sum_{m=1}^n \left[\left(e^{-\frac{t_n-t_m}{\tau_{kj}}} - e^{-\frac{t_n-1-t_m}{\tau_{kj}}} \right) \cdot P_{wf_k}(t_m) \right] \right) \right] \right\} \\ \hat{q}_j(t) &= \text{production rate of producer } j \text{ at time } t, \text{ estimated using CRM;} \\ q_j(t_0) &= \text{initial production rate of producer } j, \text{ at time } t_0; \\ w_i(t) &= \text{injection rate of injector } i \text{ at time } t; \\ P_{wf_k}(t) &= \text{BHP of producer } k \text{ at time } t; \\ P_{wf_j}(t_0) &= \text{initial BHP of producer } j \text{ at time } t_0; \\ \tau_j &= \text{producer time constant for producer } j = \left(\frac{c_t \cdot V_p}{J} \right)_j; \\ c_t &= \text{total compressibility;} \\ V_p &= \text{pore volume;} \\ J &= \text{productivity index;} \\ \lambda_{ij} &= \text{injector-producer connectivity index;} \\ \tau_{ij} &= \text{injector-producer time constant of } i\text{th injector and } j\text{th producer well-pair;} \\ \nu_{kj} &= \text{the coefficient of the BHP term, indicating producer-producer connectivity;} \\ \tau_{kj} &= \text{producer-producer time constant of } k\text{th producer and } j\text{th producer well-pair;} \\ I &= \text{total number of injectors considered;} \\ K &= \text{total number of producers considered.} \end{aligned}$$

Connectivity index, λ_{ij} , is essentially the portion of injection rate at injector i that influences production rate at producer j , thereby quantifying the relative degree of communication (or the connectivity) between injector i and producer j (Liu et al., 2019; Ogali and Orodu, 2020; Sayarpour et al., 2009; Yousefi et al., 2006). The ν_{kj} is the coefficient of the BHP Term that quantifies the effects of changing the BHPs of producers k and j on the production rate of j (Kaviani et al., 2014; Ogali and Orodu, 2020). The time constant (τ_{ij} or τ_{kj}) of a well-pair quantifies the degree of fluid storage between the wells, and the time delay of a signal between a source well (injector or producer) and a destination well (the producer of interest). The τ_j quantifies the degree of fluid storage around the producer; the inverse defines the exponential decline of initial production rate (de Holanda et al., 2018; Sayarpour et al., 2009).

Conventional approaches to fault characterization and their limitations have been presented, such as computation costs, operational constraints during tests, substantial time and data requirements. The CRM is fast, and has far fewer data requirements which are readily available, even in legacy oilfields. Connectivity indices in CRM are functions of transmissibilities (Yousefi et al., 2006). Therefore, the CRM can be used to adequately characterize faults and flow barriers in the reservoir of interest. This will require other data sources as well as diagnostic plots.

3. Diagnostic plots

Several approaches have been used in depicting the results from calibrating the CRM. One approach is the arrow (or line) diagrams, where the length of the line is used to qualitatively infer the connectivity (for λ_{ij} ’s) and the measure of dissipation between an injector-producer well-pair (for τ_{ij} ’s) (Albertoni and Lake, 2003; Kaviani et al., 2012; Soroush et al., 2014; Yousefi et al., 2005). The second approach involves using the values of the λ_{ij} ’s and τ_{ij} ’s directly to infer connectivity between wells. Another approach involves diagnostic plots.

Yousefi et al. (2006) presented two diagnostic plots: (i.) the log-log plots; and (ii.) the dynamic flow capacity plot. The log-log plot is a graphical representation of the relationship between connectivity indices and time constants, presented in log scales. It shows an inverse relationship between these parameters. Well-pairs tend to cluster or not on the log-log plot, depending on the “degree of heterogeneity” in the field of interest. However, the general trend is an inverse relationship. Ogali and Orodu (2020) used log-log plots to quality-check results from calibrating the CRM, before using the calibrated CRM to characterize the reservoir of interest.

A Flow Capacity (FC) Plot is a graphical representation of cumulative flow capacity (kh) versus cumulative storage capacity (ϕh). Initially developed for 2D vertical cross-section, non-communicating layered reservoirs, these plots are used for estimating layer injection sweep efficiency and can be used to quantitatively describe reservoir geology (Fanchi, 2010; Izgec, 2012; Yousef et al., 2006). Simply put, they were used to evaluate the relative flow of a layer due to its associated relative pore volume. The cumulative flow capacity and cumulative storage capacity are related to the permeability-thickness (kh) and porosity-thickness (ϕh) of the layers respectively. These parameters (k , ϕ and h) are typically obtained from core samples, ignoring the spatial relationships of the samples (Yousef et al., 2006).

Flow Capacity plots have also been developed from results of calibrating the CRM. These are called Dynamic Flow Capacity (dFC) plots. According to Yousef et al. (2006), the λ quantifies the flow capacity of an injector-producer well-pair; the $\lambda\tau$ product can be used to quantify the storage capacity of an injector-producer well-pair. Considering that CRM is based on dynamic data (rate and BHP data), dFC plots may better reflect the flow path distribution, degree and type of communication (through channel, high-permeability streak, matrix) between injector-producer well-pairs (Izgec, 2012).

The fraction of total flow capacity provided by a given fraction of total storage capacity for an injector-producer well-pair, can be used to infer the presence of a reservoir seal (like a sealing fault) or high-permeability streak between the well-pair, and other geological features in the reservoir. The visually-inferred slope of the dFC curve between a well-pair is used to make these inferences: steep slope indicates a fracture or high-permeability streak; gentle or near-zero slope indicates a reservoir seal (Yousef et al., 2006). If the section of the dFC curve or line is parallel to the 45° line, this signifies “effective homogeneity” between the well-pair; the fraction of total storage capacity yielded the same fraction of total flow capacity. These are summarized in Fig. 1.

Several studies (Delshad et al., 2009; Izgec, 2012; Lee et al., 2009; Yousef et al., 2006) have used the dFC plots to characterize areas of the reservoir in between wells. Although this diagnostic plot aids the reservoir characterization process, the qualitative nature of the assessment of the slopes of this curve leaves room for discrepancies in inferences. Consequently, Yousef et al. (2006) suggested that it should be combined with other sources of data for the reservoir characterization workflow.

A second limitation of dFC Plots relates to number of wells under consideration. When evaluating interactions between few wells, the dFC curve is discrete, consisting of several “straight lines”. Consequently, visual assessments of the slopes of the dFC curve for connectivity between well-pairs is feasible. However, as the number of well-pairs

increases, the dFC curve becomes less discrete, approaching a continuous curve. Consequently, visual inspection of the slopes is no longer feasible. Thirdly, even when few wells are considered, it is impractical to evaluate the degree of communication between well-pairs that are closely spaced on the dFC Plot. Therefore, a diagnostic plot that addresses these limitations is necessary in the reservoir characterization workflow involving the CRM.

Combining calibrated CRM with geological data can provide more understanding on geological characteristics influencing connectivity (Soroush et al., 2014). Consequently, the results from calibrating CRM were combined with diagnostic plots, geological data and well data in order to characterize faults and identify flow barriers in a real field.

4. Methodology

Three cases involving waterflooded synfields were evaluated using the CRM. In each case, the CRM was calibrated using historical injection rates and liquid production rates. The calibrated CRM was thereafter used to develop diagnostic plots, such as the dynamic Flow Capacity (dFC) Plots, for evaluating the “heterogeneity” of the synfields. Thereafter, the CRM and diagnostic plots were applied to a Far East Oil Field (FEOF). No BHP data was available in FEOF. Combining the calibrated CRM, geologic data, wells data and diagnostic plots, two selected faults in FEOF were characterized and, other flow barriers around the faults identified. A program developed using MathWorks MATLAB™ was used in calibrating CRM, via multivariate non-linear optimization.

5. Workflow for capacitance-resistance model

In this study, the CRM was implemented such that, the injection and BHP terms in the model were included only if these data sets were available. The BHP data were unavailable in this study. Consequently, only production and injection terms in the CRM (τ_j , λ_{ij} and τ_{ij}) were optimized. Unlike the step-wise optimization approach proposed by Yousef et al. (2005), simultaneous optimization of all CRM parameters was implemented in this study, subject to several constraints.

Three optimization constraints were implemented. In one constraint, the range of values for the λ_{ij} of each injector-producer well-pair is between 0.0 and 1.0 ($0 \leq \lambda_{ij} \leq 1$). For the second constraint, the sum of λ_{ij} for all injector-producer well-pairs of an injector was less than or equal to 1.0 (Kaviani et al., 2012). The time constant should be greater than the sampling rate of the data in order to determine the medium’s properties in the control volume (Yousef et al., 2006). Lower and upper bounds of time constants ($LB\tau$ and $UB\tau$ respectively) were specified.

The consistency in the estimations of λ and τ improves with increasing sample size (number of data points). Large sample sizes (about four times the number of CRM unknowns) are therefore recommended to achieve optimum quality in CRM results (Sayarpour et al., 2009). However, Kaviani et al. (2012) stated that λ and τ estimations are mostly consistent with small sample sizes and low-to-moderate amounts of noise in the data. Consequently, the size of the historical data was compared to the number of CRM unknowns, and appropriate time ranges were selected in order to capture interwell interactions as well as identify flow barriers.

The CRM parameters of all producers were optimized simultaneously using multivariate non-linear optimization, by concurrently matching the production history of all producers. The Objective Function ($ObjFcn$) to be minimized is presented in Equation (3).

$$ObjFcn = \frac{1}{N \cdot K} \cdot \left\{ \sum_{j=1}^K \left[\sum_{n=1}^N \left(q_j^{(n)} - \hat{q}_j^{(n)} \right)^2 \right] \right\} \quad (3)$$

Where: N = total number of time-steps (or periods); K = total number of producers; $q_j^{(n)}$ = observed production rate of j th producer at n th time-step (or period); $\hat{q}_j^{(n)}$ = CRM-estimated production rate of j th producer at

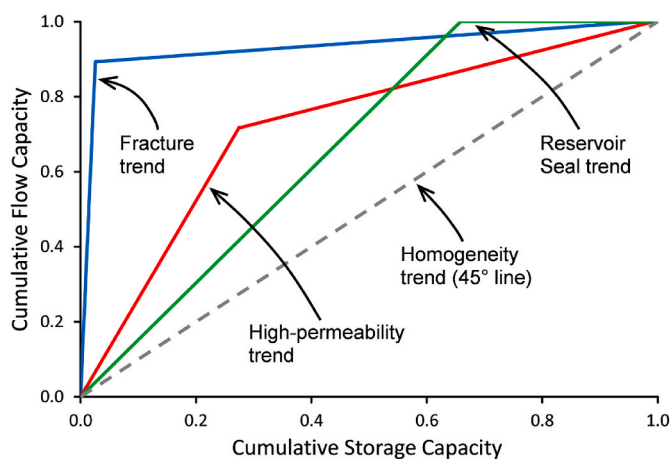


Fig. 1. Summary of Dynamic Flow Capacity Curves depicting different geological conditions in reservoirs (Yousef et al., 2006).

n th time-step (or period).

Three measures have been proposed in the literature for evaluating the performance of the CRM. These are: (i.) the coefficient of determination (or correlation coefficient, R^2); (ii.) the asymmetric coefficient (A); and (iii.) the modified coefficient of efficiency (E_m). The R^2 evaluates the “goodness of fit” of the CRM by comparing the CRM-generated production rates and the observed production rates, using Equation (4) (Legates and McCabe, 1999). The range of R^2 is 0.0 to 1.0. Several studies (Albertoni and Lake, 2003; Dinh and Tiab, 2008) used the asymmetric coefficient on symmetric, homogeneous and isotropic synthetic reservoirs. This is because, Jensen et al. (1997) stated that R^2 is a weak indicator of “goodness of fit”. However, the asymmetric coefficient cannot be applied to heterogeneous and anisotropic reservoirs. The E_m , obtained using Equation (5), ranges from $-\infty$ to 1.0 with higher values indicating better agreement between observed and estimated values (Legates and McCabe, 1999). Dinh and Tiab (2008) applied the E_m , although referring to it as “coefficient of determination”. In this study, R^2 and E_m were used in evaluating the performance of the CRM. Both measures showed similar trends and thus, only the R^2 was reported.

$$R_j^2 = \left\{ \frac{\sum_{n=1}^N \left\{ \left(q_j^{(n)} - \bar{q}_j \right) \times \left(\hat{q}_j^{(n)} - \bar{\hat{q}}_j \right) \right\}}{\left\{ \left[\sum_{n=1}^N \left(q_j^{(n)} - \bar{q}_j \right)^2 \right] \times \left[\sum_{n=1}^N \left(\hat{q}_j^{(n)} - \bar{\hat{q}}_j \right)^2 \right] \right\}^{0.5}} \right\}^2 \quad (4)$$

$$E_{m,j} = 1.0 - \left\{ \frac{\sum_{n=1}^N \left| q_j^{(n)} - \hat{q}_j^{(n)} \right|}{\sum_{n=1}^N \left| q_j^{(n)} - \bar{q}_j \right|} \right\} \quad (5)$$

Where: $q_j^{(n)}$ = observed production rate of j th producer at n th time-step (or period); $\hat{q}_j^{(n)}$ = CRM-estimated production rate of j th producer at n th time-step (or period); \bar{q}_j = average of all observed production rates of j th producer during the history; $\bar{\hat{q}}_j$ = average of all CRM-generated production rates of j th producer during the history; N = total number of time-steps.

The application of CRM to synfields or real fields is based on a

generic workflow. Ogali and Orodu (2020) presented a generic workflow for calibrating the CRM, which involves several steps: (i.) selection of wells and time window (if necessary); (ii.) data collation within the time window; (iii.) parameter initialization; (iv.) non-linear optimization; (v.) evaluation of CRM-estimated rates. A flow chart for calibrating the CRM using historical data is presented in Fig. 2. The results from this workflow are optimized CRM parameters and CRM-estimated liquid production rates.

An Inference Guide developed by Ogali and Orodu (2020) for evaluating the level of connectivity between an injector-producer well-pair using optimized values of λ 's and τ 's, is presented in Table 1. In this study, some of the optimized CRM parameters were used to develop diagnostic plots and subsequently, evaluate interwell connectivities and characterize the fields of interest.

6. Diagnostic plots used in inferring connectivities between wells

The optimized CRM parameters used to identify faults, flow barriers and high-permeability trends are the injector-producer connectivity indices (λ_{ij}) and time constant (τ_{ij}). Log-log plots were created to quality-

Table 1

Inference Guide on Well-pair Connectivity based on Ranges of λ_{ij} 's and τ_{ij} 's (Ogali and Orodu, 2020).

S/No.	Ranges for CRM Parameters	Inferences on Well-pair Connectivity
1.	$\lambda_{ij} \approx 0$; $\tau_{ij} \rightarrow LB_\tau$	No connectivity between injector-producer well-pair.
2.	$\lambda_{ij} \approx 0$; $\tau_{ij} \rightarrow \infty$	No connectivity between injector-producer well-pair.
3.	$\lambda_{ij} > 0$; $\tau_{ij} > LB_\tau$	Communication between injector-producer well-pair.
	(a.) $0 < \lambda_{ij} \leq 0.02$	Insignificant Connectivity
	(b.) $0.02 < \lambda_{ij} \leq 0.1$	Negligible Connectivity
	(c.) $0.1 < \lambda_{ij} \leq 0.2$	Significant Connectivity
	(d.) $\lambda_{ij} > 0.2$	Strong Connectivity
4.	$\lambda_{ij} > 0$; $\tau_{ij} \approx LB_\tau$	Apparent connectivity which is likely a false positive.

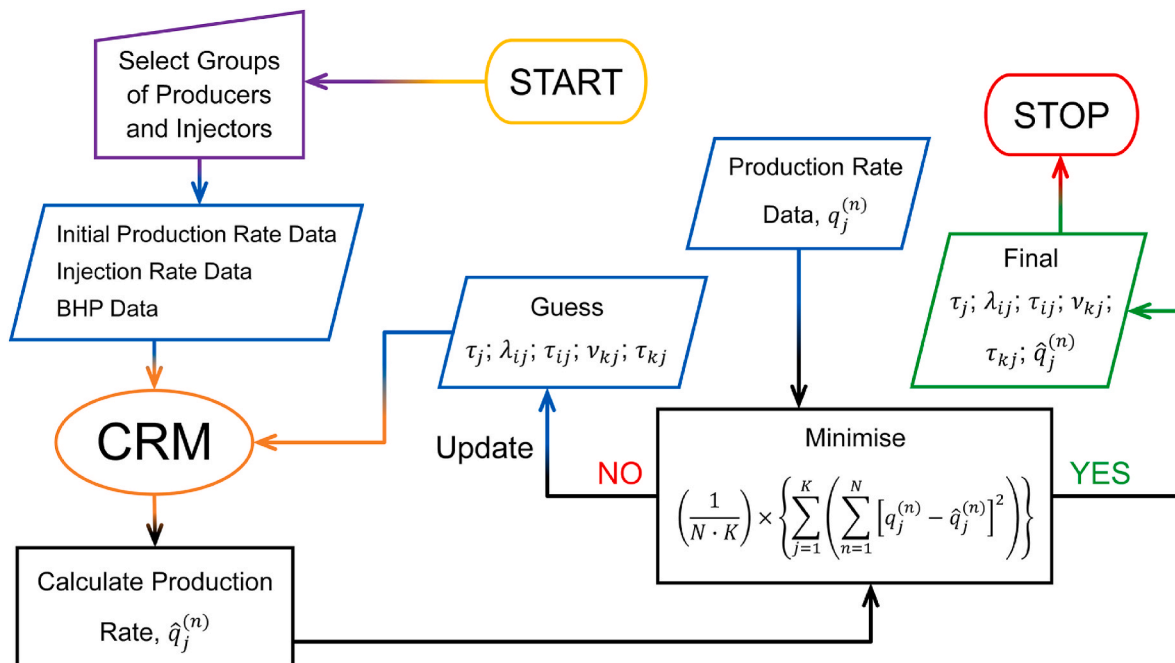


Fig. 2. Flow chart for calibrating the Capacitance-Resistance Model (Ogali and Orodu, 2020).

check the results from calibrating the CRM, ensuring that they were viable for assessing interwell connectivities around the selected faults in FEOF. Dynamic Flow Capacity (dFC) Plots were generated using λ_{ij} 's and τ_{ij} 's. This involved computing the cumulative flow capacity (F_x) and cumulative storage capacity (C_x) using Equations (6) and (7) respectively.

$$F_x = \frac{\sum_{i=1}^x \lambda_{ij}}{\sum_{i=1}^I \lambda_{ij}} \quad (6)$$

$$C_x = \frac{\sum_{i=1}^x (\lambda_{ij} \bullet \tau_{ij})}{\sum_{i=1}^I (\lambda_{ij} \bullet \tau_{ij})} \quad (7)$$

Where: F_x = cumulative flow capacity of xth well-pair index; C_x = cumulative storage capacity of xth well-pair index. The data were arranged in order of decreasing $1/\tau$, such that $x = 1$ is the injector-producer well-pair with the smallest τ and $x = I$ is the well-pair with the largest τ . The dFC Plots can be developed from a producer standpoint (assessing interactions between a selected producer and surrounding injectors) or an injector standpoint (assessing interactions or influences between a selected injector and surrounding producers) (Yousef et al., 2006). In this study, it was developed from a producer standpoint.

Two limitations in applying the dFC Plots are; (i.) the discrepancies that can occur from making inferences based on visual inspection of the slopes of the dFC curve; (ii.) the increasing inability to make such inferences as the number of wells under consideration increases. Consequently, a new diagnostic plot that addresses these limitations is necessary.

Lake (1989) discussed two common measures of heterogeneity: the Lorenz coefficient (L_c) and the Dysktra-Parson coefficient (V_{DP}). The Lorenz coefficient is computed from the Lorenz curve, which is based on the static flow capacity (FC) plot. This coefficient is defined as the area between the FC curve and a 45° line (homogeneous FC curve), obtained using Equation (8). Using the FC curve, the V_{DP} is computed with Equation (9), where F' is the gradient of the FC curve at the specified cumulative storage capacities. Both measures of heterogeneity range from 0.0 (homogenous) to 1.0 (infinitely heterogeneous). Another measure of heterogeneity is the Koval Heterogeneity Factor (H_K), which directly relates to flow in permeable media (Koval, 1963). The range of H_K is 1.0 (homogeneous) to infinity (infinitely heterogeneous), and can be obtained from the FC curve using Equation (10) (Lake, 1989).

$$L_c = 2 \left\{ \int_0^1 F dC - \frac{1}{2} \right\} \quad (8)$$

$$V_{DP} = \frac{(F')_{C=0.5} - (F')_{C=0.841}}{(F')_{C=0.5}} \quad (9)$$

$$H_K = \left(\frac{1-C}{C} \right) \bullet \left(\frac{F}{1-F} \right) \quad (10)$$

A modified H_K (H_K^*), obtained using Equation (11), was developed to evaluate interwell relations from the dFC Plots. The dF_x is the difference between the cumulative flow capacities of the xth well-pair and the (x-1)th well-pair; the dC_x is the difference in cumulative storage capacities of the xth well-pair and the (x-1)th well-pair. The range was 0.0 to infinity, indicating zero communication (likely presence of a sealing flow barrier) and instantaneous communication (likely presence of infinite-conductivity fractures) between the well-pair respectively. A well-pair in which the fraction of cumulative storage capacity yields the same fraction of cumulative flow capacity, has a H_K^* of 1.0. The H_K^* therefore quantified degree of communication based on flow capacities and storage capacities but, the range was too wide.

$$H_K^* = \left(\frac{1-dC_x}{dC_x} \right) \bullet \left(\frac{dF_x}{1-dF_x} \right) = \left\{ \frac{1-(C_x-C_{x-1})}{C_x-C_{x-1}} \right\} \bullet \left\{ \frac{F_x-F_{x-1}}{1-(F_x-F_{x-1})} \right\} \quad (11)$$

An index was developed based partly on the dFC workflow, called the Flow-Storage Index (I_{FS}). The range of I_{FS} is 0.0–1.0 indicating zero communication (likely presence of a sealing flow barrier) and instantaneous communication (likely presence of infinite-conductivity fractures) between the well-pair respectively. A well-pair with I_{FS} around 0.5 means that the fraction of cumulative storage capacity yields similar fraction of cumulative flow capacity, which is indicative of “effective” homogeneity in between the well-pair. The I_{FS} is computed using Equation (12), and has two limits.

$$I_{FS} = \frac{1}{4} \bullet \left\{ 2 + \log \left(\frac{dF_x}{dC_x} \right) \right\} = \frac{1}{4} \bullet \left\{ 2 + \log \left(\frac{F_x - F_{x-1}}{C_x - C_{x-1}} \right) \right\} \quad (12)$$

$$\lim_{\frac{dF_x}{dC_x} \rightarrow 0.01} I_{FS} = 0.0; \quad \lim_{\frac{dF_x}{dC_x} \rightarrow 100} I_{FS} = 1.0$$

Using this index, the I_{FS} Plot (a new diagnostic plot) is developed. Connectivity indices and time constants may each vary within one order of magnitude, typically for homogeneous synfields, as will be illustrated later in this study. However, in real fields, there is a tendency for these CRM parameters to vary in several orders of magnitude. Consequently, the limits in Equation (12) are necessary in making reasonable inferences on interwell communication. An injector-producer well-pair with $\lambda_{ij} = 0.000$ will have $I_{FS} = 0.000$. In making deductions on interwell communication, especially in real fields, the I_{FS} is combined with time constants of the well-pair. This is in part because, the time constants tend to provide more insight into the geological conditions in between wells (Yousef et al., 2006).

One advantage of the I_{FS} Plot is its ability to display the selected well's “perspective” in relation to other wells in the field. This is because, if I_{FS} Plots of producers are generated for instance, the surrounding injectors can be arranged in the same sequence for each producer. Consequently, it is possible to obtain each producer's “view” of well interactions in the field in comparison to other producers, by evaluating the profiles in the I_{FS} Plots. Both diagnostic plots (dFC Plots and I_{FS} Plots) were combined with CRM results and other data sets in characterizing faults and identifying flow barriers in a real field.

An Inference Guide is therefore developed for utilizing the I_{FS} plots in determining interwell communication and consequently, characterizing a reservoir of interest. This is presented in Fig. 3. Using this guide, evaluations of interwell communication was carried out, and the results used to characterize the reservoir of interest.

7. Validation of CRM and diagnostic plots in evaluating interwell communication

Capacitance-Resistance Model and Diagnostic Plots were validated using three cases involving synfields, to quantify the degree of communication between the wells and consequently, identify geological conditions in the synfields. All synfields involve five (5) injectors and four (4) producers (all vertical wells) in 5-spot pattern waterflood, similar to the well placement consistently used in CRM-related studies (Kaviani et al., 2012; Mohamdally et al., 2018; Sayarpour et al., 2009; Yousef et al., 2005). The cases are:

1. **Case A.** This involves a Homogeneous Synfield with undersaturated oil. All producers have constant and equal bottomhole flowing pressure (BHPs) throughout the simulation period. Shortest injector-producer distance is 800 ft. The synfield dimensions are 31 × 31 × 5; the grid sizes are 80 ft × 80 ft × 12 ft. The oil, water and rock compressibilities are 5 × 10⁻⁶ psi⁻¹, 1 × 10⁻⁶ psi⁻¹ and 1 × 10⁻⁶ psi⁻¹ respectively. The end-point oil-water mobility ratio is unity.

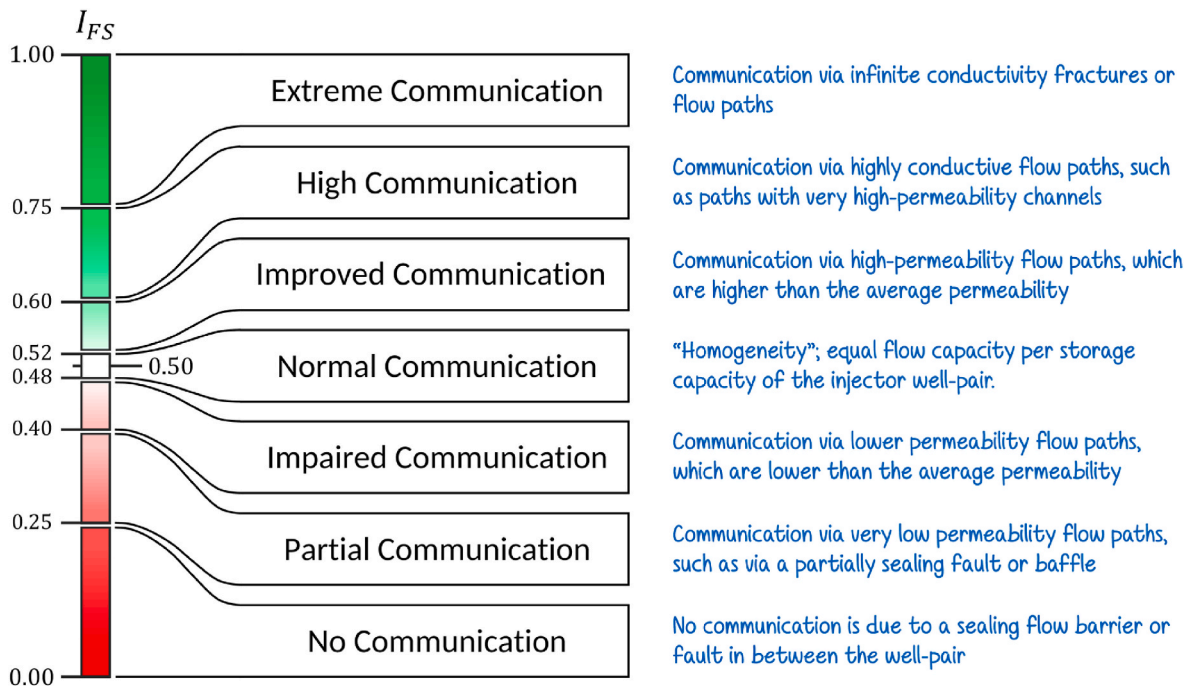


Fig. 3. Inference guide for flow storage index (I_{FS}).

Porosity is 18%, homogeneous horizontal permeability of 40 mD and vertical permeability of 4 mD. Injection Rates of injectors are presented in Figure A1; production rates of producers in this case are presented in Figure A2. The simulation spans 100 months, with monthly rate data, resulting in 100 data points.

- Case B.** This involves a Homogeneous Synfield mostly similar to Case A but, with homogeneous horizontal permeability of 5 mD and vertical permeability of 0.5 mD. There are two high-permeability fractures: one fracture between injector I-01 and producer P-01 with permeability of 1000 mD, and the other fracture is between injector I-03 and P-04 with permeability of 500 mD. The end-point oil-water mobility ratio is unity. The injection rates of injectors are the same as in Case A. The simulation spans 100 months, with monthly rate data, yielding 100 data points.
- Case C.** This also involves a Homogeneous Synfield mostly similar to Case A with homogeneous horizontal permeability is 40 mD with vertical permeability of 4 mD. There are no high-permeability fractures. However, a sealing fault completely divides the synfield into two compartments. The end-point oil-water mobility ratio is unity. The injection rates of injectors are the same as in Case A. The simulation spans 100 months, with monthly rate data, yielding 100 data points.

These cases are similar to those presented by Al-Yousef (2006). All wells in each case were perforated in all five layers. A summary of the synfield characteristics for each case is presented in Table 2. The well placements, as well as variations in geological conditions imposed in some of the cases, are summarized in Fig. 4. Total liquid production rates for all three synfield cases are presented in Figure A3. These synfields were used to validate the CRM and Diagnostic Plots before applying these tools to a real field, the Far East Oil Field (FEOF).

In this study, the units of all τ 's were months, similar to the sampling rate in the historical data for all cases and FEOF. For the synfield cases however, the range of values for all τ 's was a lower bound ($LB\tau$) of 0.6 month to an upper bound ($UB\tau$) of 10,000 months. In the FEOF, the $LB\tau$ was $1/30.44$ month (equivalent to 1 day) and the $UB\tau$ was $(10,000 \times N)$ months, where N is the total number of data points.

Table 2

Summary of Synfield Cases used to validate CRM and the Diagnostic Plots.

PARAMETER	CASE A	CASE B	CASE C
Porosity, [%]	18	18	18
Horizontal Permeability, [mD]	40	5	40
Vertical Permeability, [mD]	4	0.5	4
Oil Compressibility, [psi^{-1}]	5×10^{-6}	5×10^{-6}	5×10^{-6}
Water Compressibility, [psi^{-1}]	1×10^{-6}	1×10^{-6}	1×10^{-6}
Rock Compressibility, [psi^{-1}]	1×10^{-6}	1×10^{-6}	1×10^{-6}
Model Dimensions	$31 \times 31 \times 5$	$31 \times 31 \times 5$	$31 \times 31 \times 5$
Grid Size, [ft]	$80 \times 80 \times 12$	$80 \times 80 \times 12$	$80 \times 80 \times 12$
Injector-Producer Distance, [ft]	800	800	800
Data Points used	100	100	100
Fractures	NONE	2 Fractures	NONE
Flow Barriers	NONE	NONE	1 Sealing Fault

8. Workflow for fault and reservoir characterization using the calibrated CRM, geological and well data

The CRM and Diagnostic Plots were used to characterize selected faults and identify other flow barriers in a real field. Based on the historical data in relation to the number of CRM unknowns necessary for fault characterization, an appropriate time window in history was selected. This coincided with periods when most of the selected wells were active during the history. However, not all producers were active at the beginning of the selected time window. For such producers, the initial production rate based on the selected time window (a parameter necessary in calibrating the CRM) will be zero. It was therefore possible to have zero initial production rates with corresponding large connectivity indices or, zero connectivity indices with corresponding large initial production rates (Altaheini et al., 2016; Sayarpour et al., 2009).

In this study, the first production rate for a producer within the time window selected, was used as the producer's "initial production rate", $q_j(t_0)$, which is a variable required in the Production Term of the CRM. For each producer, the time step for this "initial production rate" is the initial time-step (t_0), meaning that t_0 varied for each producer. Injectors and producers on both sides of the fault of interest were selected, in order to assess communication across the fault. Several criteria were

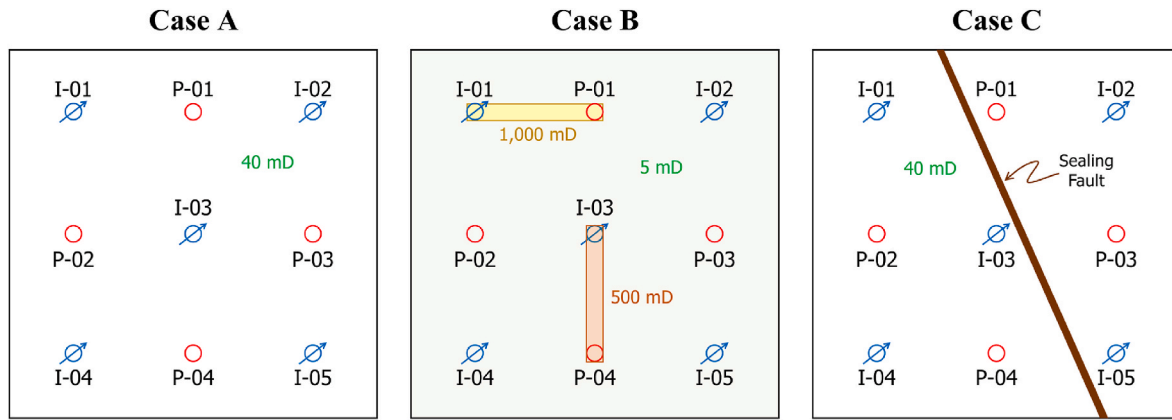


Fig. 4. Well Placements and Geologic Conditions for Synfield Cases used in validating the CRM and Diagnostic Plots.

used in the well selection process, which is discussed later. All CRM parameters for all producers were evaluated simultaneously, irrespective of when the producer became active during the selected time window.

The CRM was calibrated using the historical data from the selected time window. Thereafter, diagnostic plots derived from calibrated CRM were combined with CRM, as well as Geological and Wells Data to characterize the selected faults, identify flow barriers and consequently, characterize the field of interest. The generic workflow for this process involved several steps:

- S1. Selection of Wells and Calibration of CRM.** This involves several processes: (i.) wells around the fault(s) are selected systematically; and (ii.) historical rate data (and BHP data if available) are used to calibrate the CRM.
- S2. Creation of Diagnostic Plots.** Using results from CRM calibration, diagnostic plots are developed which aid the fault characterization process.
- S3. Collation of Geological Data and Wells Data.** Data from geological and well sources are collated and systematically summarized for integration in the characterization workflow.

S4. Combination of All Data Sources for Fault Characterization.

The calibrated CRM and diagnostic plots are combined with geological and wells data for the fault characterization process. Using the calibrated CRM parameters, inferences on degrees of communication between wells in the real field, were based on the guide presented by Ogali and Orodu (2020). Based on the results of characterization, the structural map of the field is updated.

A flow chart for characterizing faults and identifying flow barriers is presented in Fig. 5. This workflow yields adequately characterized faults and flow barriers in the field of interest, using historical rate data, geological data and wells data. This workflow was implemented in this study, using data from a Far East Oil Field (FEOF).

9. Reservoir description of the far east oil field (FEOF)

The Far East Oil Field (FEOF) is in the South sub-block of a block in the Far East. It is separated from the North sub-block by a major sealing fault in the northeast direction (Fig. 6). The South sub-block comprises of anticlinal oil-bearing strata dipping north-westward with relatively small sand bodies and poor connectivities, and compartmentalized by a

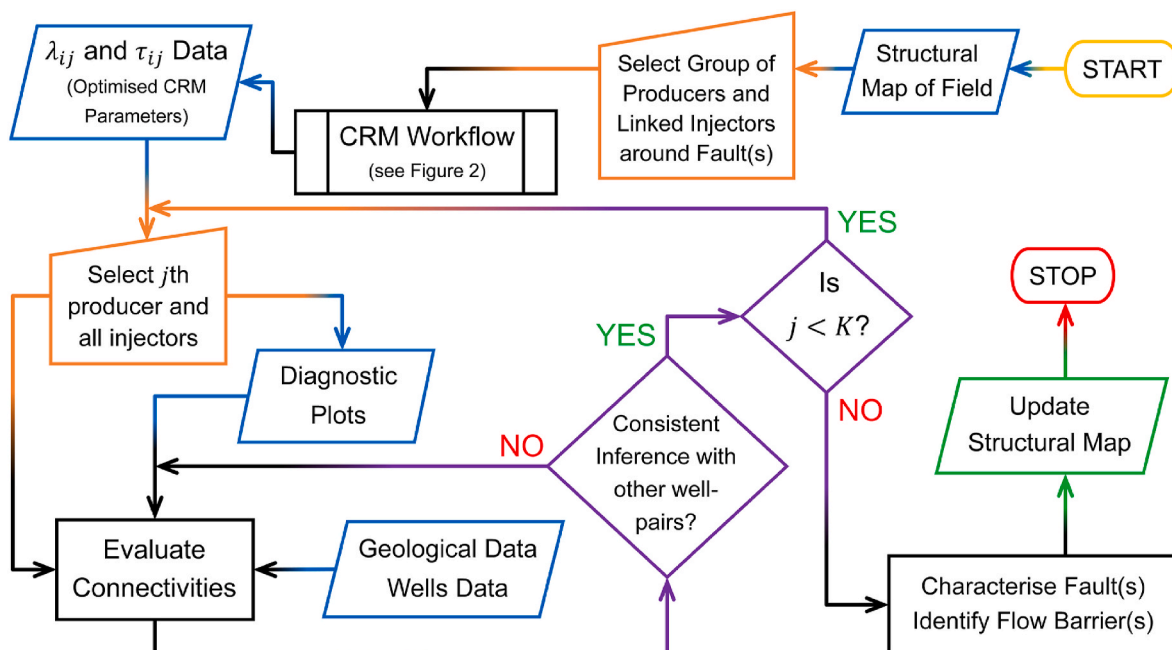


Fig. 5. Flow chart for Fault Characterization using CRM, Diagnostic Plots, Geological Data and Wells Data.

Facies 1: Flood Plain (silt, fine sand and mud);
 Facies 2: Lake (lacustrine mud), Flood Basin (mud) and Flood Basin-Distributary Channel (mud);
 Facies 3: Levee (river side silty-sand);
 Facies 4: Mouth Bar;
 Facies 5: Crevasse Splay Sand;
 Facies 6: Main Channel (fluvial environment), Channel Sand (deltaic plain) and Channel Sand (deltaic front).

The FEOF was subdivided into three zones of 22 layers (*I.Layer* Nomenclature), based on sequence stratigraphy (Orodu, 2009). Some of these layers were combined, resulting in three zones and 17 layers (*II.Layer* Nomenclature). Based on the unpublished report, the perforation intervals of the wells in FEOF were reported using the *I.Layer* nomenclature. Due to data availability of “effective oil thickness”, facies variations throughout FEOF were reported using the *II.Layer* nomenclature. The layers in FEOF are heterogeneous with large variations in reservoir thickness (0.74 m–44 m) and poor horizontal connectivity (Orodu, 2009). The 3D Facies Model showing all 17 layers, as well as only Layer 1 and Layer 12 are presented in Fig. 7. The net pay thickness maps of Layers 1 and 12 are presented in Fig. 8a and b respectively. As shown, there are substantial variations in thickness laterally and with depth.

Two selected faults in FEOF, labelled Fault “A” and Fault “B”, were assessed using results from calibrating the CRM. Fault “A” has throws ranging from less than 5 m near the northern end of the fault to a maximum of about 30 m in the section around wells J37–63, J38–62 and J37-61. Fault “B” has throws with range of less than 5 m in the section near well J42-66 to about 15 m in the section near wells J37–67, J38–66 and J37-69 (see Fig. 6). Net pay intersection map showing several layers, their thicknesses and the intersection of Faults “A” and “B” are presented in Fig. 9.

For each fault, wells on either side of the fault were systematically selected. For each well, the facies for each layer were based on data from the Facies Map and the *II.Layer* nomenclature. Using the *I.Layer* nomenclature, data on perforation intervals of the selected wells were collated. The perforated layers of each injector were colour-coded; each

colour depicting the range of reported injectivity of the well at that layer. Consequently, geologic data (the summarized facies models) and wells data (perforation data for wells) were combined with the calibrated CRM and Diagnostic Plots to characterize the selected faults in FEOF, and identify sealing baffles (flow barriers that are not due to facies discontinuity).

12. Selection of wells and other data sets for characterizing fault “a” in FEOF

Injectors and producers were selected on both sides of Fault “A”. The selection of these wells was based on cumulative water injection and cumulative liquid (oil + water) production respectively, shown in Fig. 10. Red and blue indicate cumulative oil and water production respectively; light-blue lines indicate cumulative water injection. Some wells with relatively low cumulative production or injection were chosen in some parts of the selected faults because, those were the only wells available for use in those parts of the faults. The likely injector-producer interactions in FEOF are also presented as black arrows but, these were not used in this study. It is important to note that none of the injectors or producers were active throughout the history.

Fault “A” is indicated in Figs. 7b and 11. The FEOF structural map showing the area of the selected wells around Fault “A” is presented in Fig. 11. Based on cumulative water injection for injectors and cumulative liquid production for producers, 24 wells (8 injectors and 16 producers) were initially selected for characterizing Fault “A”. Historical injection and production data of wells spanned 299 months, resulting in 299 data points. However, the wells were mostly active between the 55th month and the 252 nd month, resulting in 198 data points. Using only Production and Injection Terms in CRM, there will be 272 CRM parameters to optimize, which will possibly lead to sub-optimal results.

Consequently, 20 wells were selected for the characterization process: five injectors and six producers west of Fault “A”; three injectors and six producers east of the fault. Each well was assigned Arbitrary String Numbers (ASN), thereby identifying periods during the history when each well was active. The ASNs of 1–8 were assigned to the eight

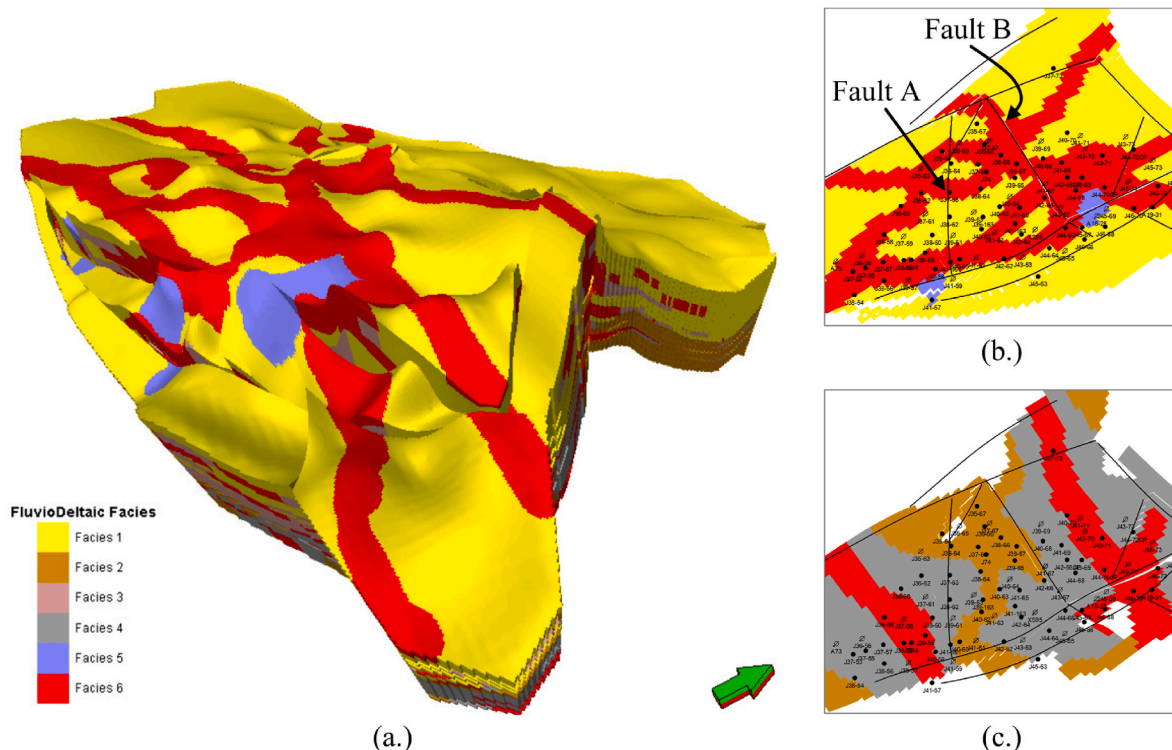


Fig. 7. Facies Map of Far East Oil Field (FEOF), showing: (a.) all 17 layers; (b.) only Layer 1; and (c.) only Layer 12 (Ogali and Orodu, 2020; Orodu, 2009).

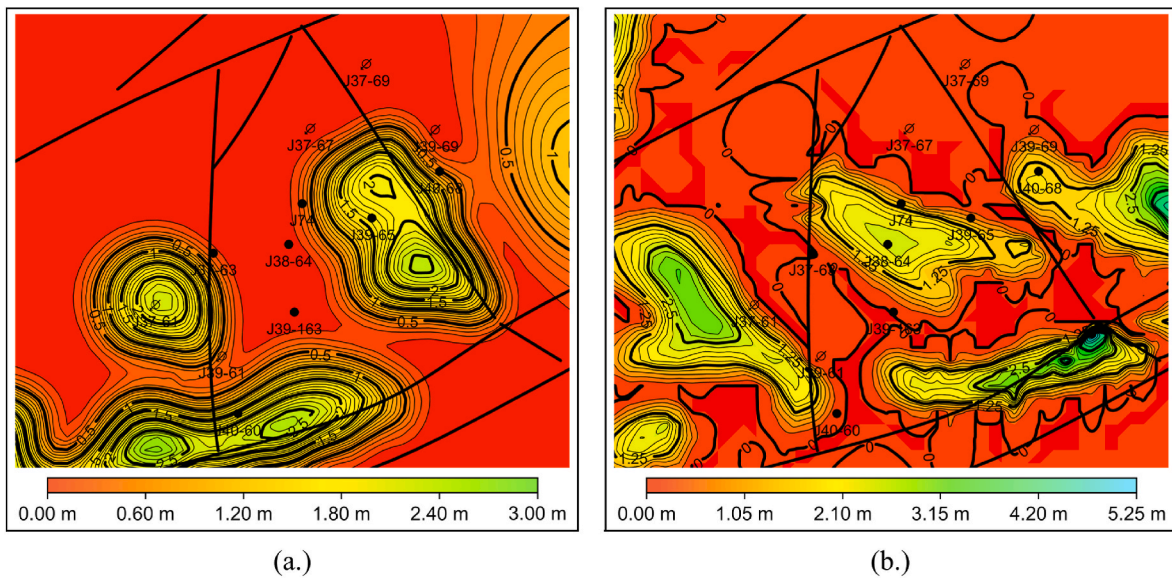


Fig. 8. Thickness Maps for: (a.) Layer 1; and (b.) Layer 12 (unpublished report).

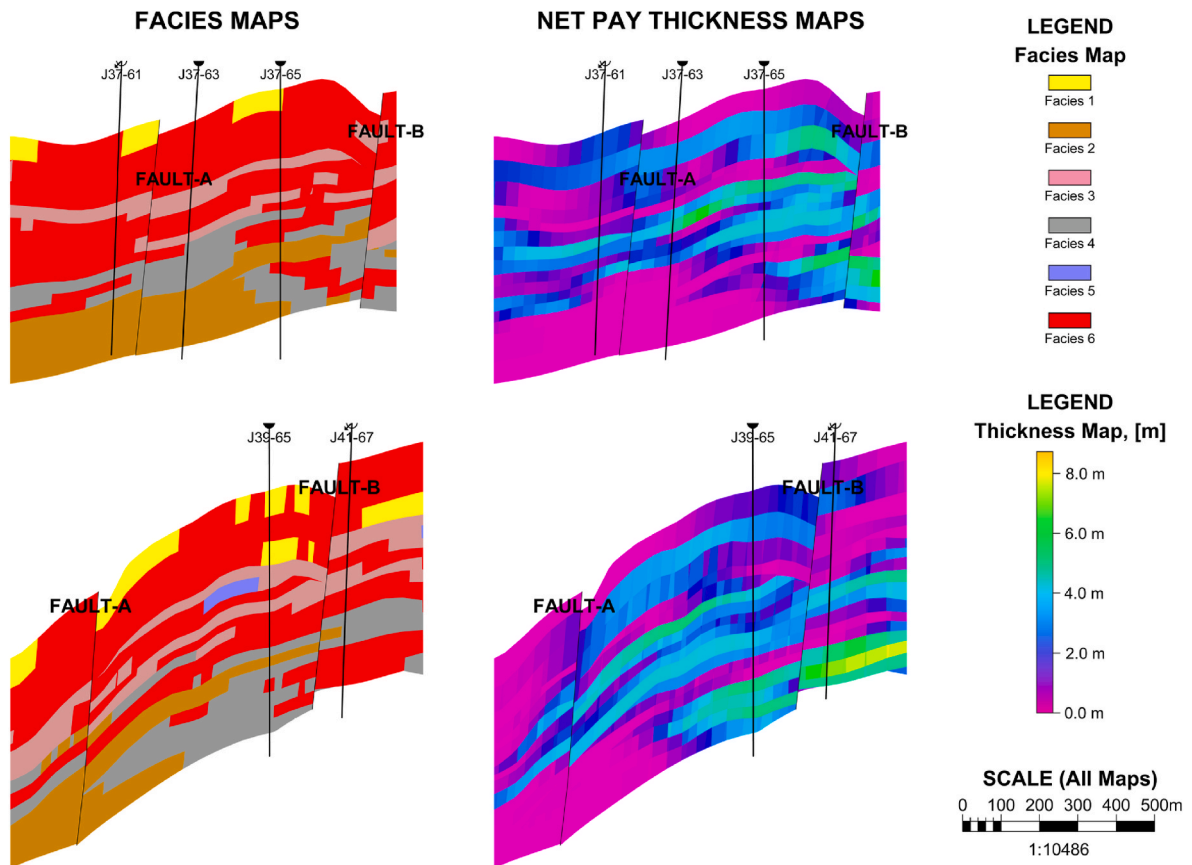


Fig. 9. Snapshots of Facies and corresponding Net Pay Thickness Intersection Maps around Faults “A” and “B”.

injectors while, 11 to 22 were assigned to the twelve producers. The ASN assignments are summarized in Fig. 12a, with blue indicating that the well is west of Fault “A” and red indicates wells east of the fault. A plot of ASN versus Time (in months) is presented in Fig. 12b, showing months when the selected wells were active during the history.

Using the Facies Map of FEOF (see Fig. 7), the facies of the selected wells in each of the 17 layers (*ILayer* nomenclature) were collated, and are presented in Fig. 13. This was necessary to incorporate the geology

of FEOF in the characterization of Fault “A”. However, the indicated facies in each layer of the selected wells are not indicative of facies in between the wells. Two instances of facies variation are presented for Layers 1 and 12 in Fig. 7b and c respectively, showing lateral variation of facies in FEOF. Based on the *ILayer* nomenclature, data on perforation intervals of the selected wells (injectors and producers), as well as results from injectivity tests on injectors, were also collated and presented in Fig. 14. Only the injectors are colour-coded in Fig. 14, with each colour

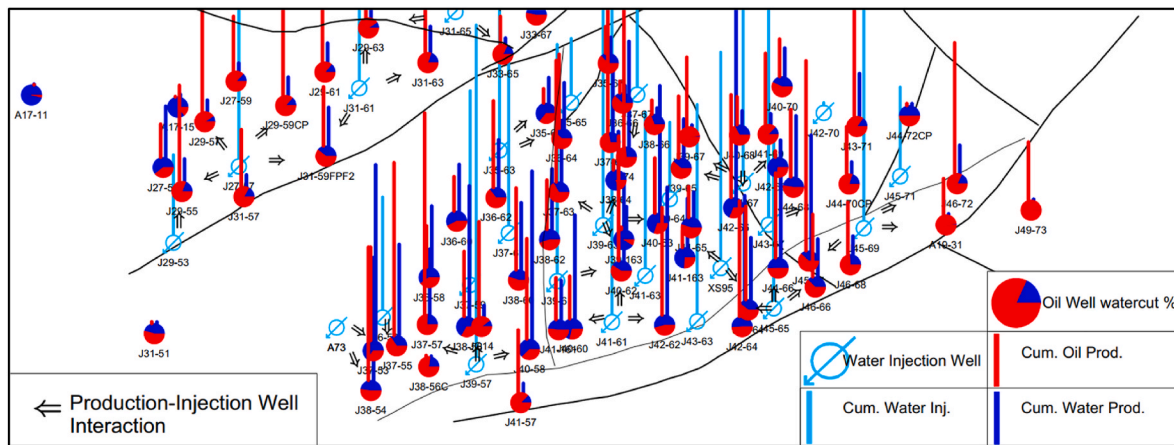


Fig. 10. Cumulative production and injection for wells in FEOF (Orodu, 2009).

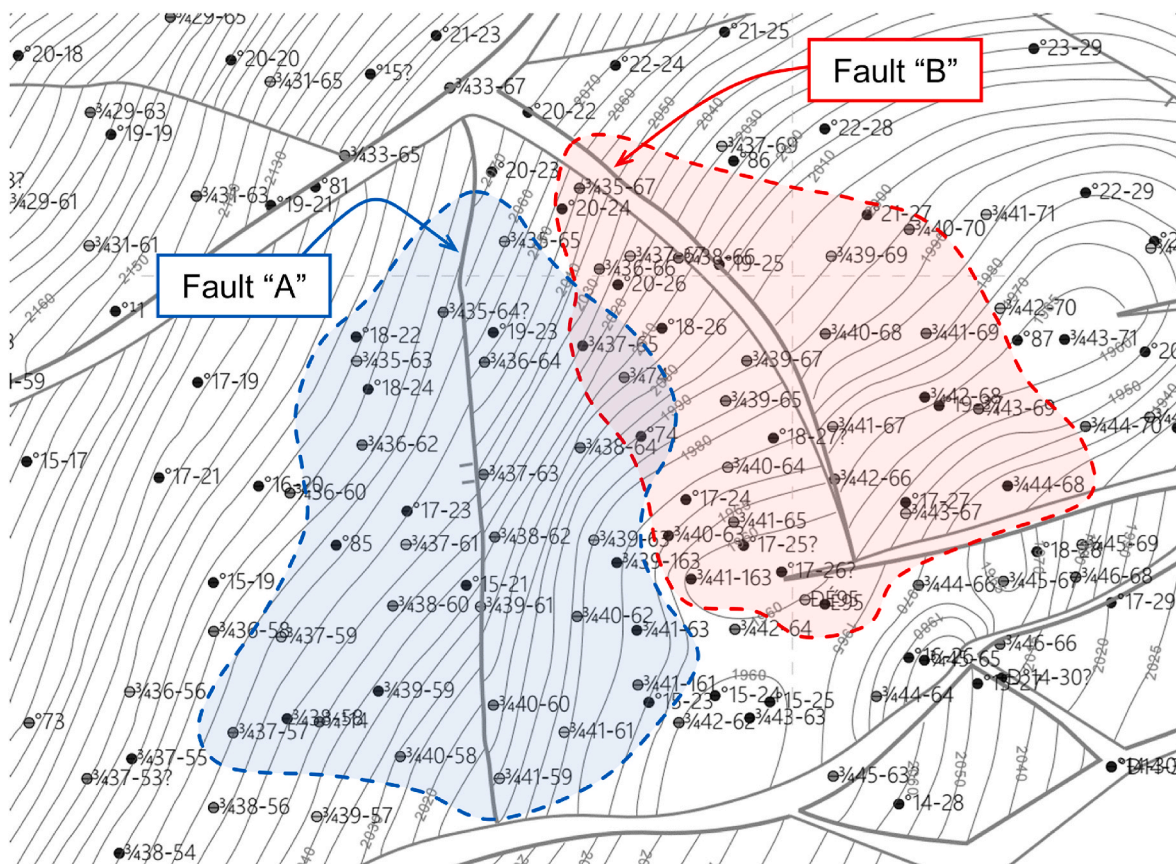


Fig. 11. Structural Map of FEOF, showing area of selected wells around Fault “A” (light-blue shaded area) and Fault “B” (light-red shaded area) in FEOF. (For interpretation of the references to colour in this figure legend, the reader is referred to the Web version of this article.)

representing the reported injectivity of the well in that perforation interval.

Simply put, the optimized CRM parameters were combined with geological data (summarized facies model) and well data (perforation data of selected wells and injectivity data of selected injectors) to characterize Fault “A” and identify sealing baffles (flow barriers not due to facies discontinuity). This involved evaluating the interwell connectivities in relation to variations in facies and perforation intervals between wells.

13. Selection of wells and other data sets for characterizing fault “B” in FEOF

Fault “B” is indicated in Figs. 7b and 11. The FEOF structural map showing the area of the selected wells around Fault “B” is presented in Fig. 11. Based on cumulative water injection and cumulative liquid (oil + water) production of injectors and producers respectively, as shown in Figs. 10 and 22 wells (6 injectors and 16 producers) were selected on both sides of Fault “B”. Four producers in the selection were, at some point in the history, converted to injectors. Such wells were represented as two wells. For instance, J37-67P represents well J37-67 when it was a

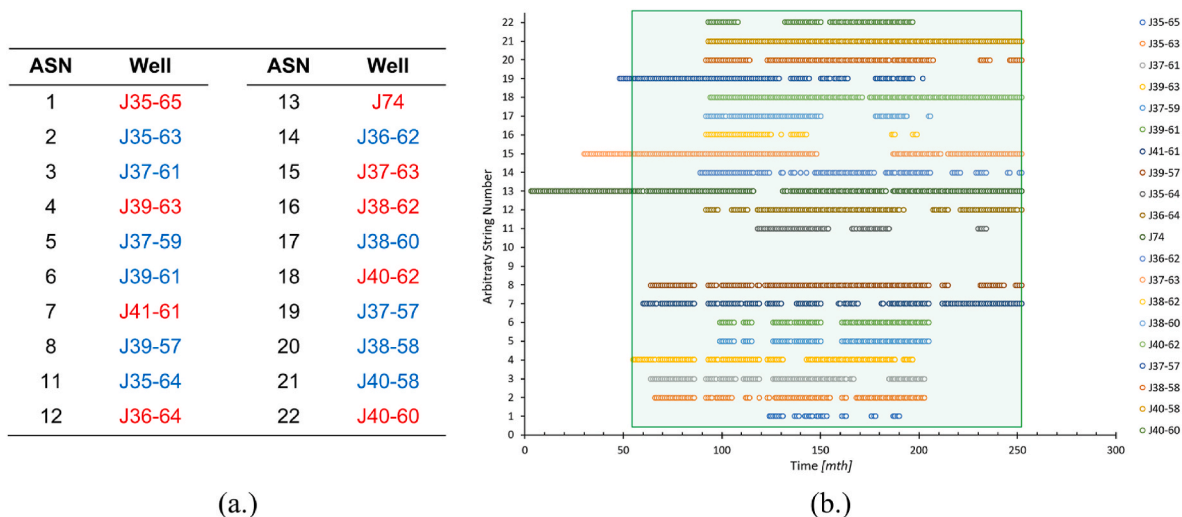


Fig. 12. (a.) Arbitrary String Numbers (ASN) assigned to Selected Wells around Fault “A” (blue wells are west of fault, red wells are east of fault); (b.) Plot of ASN versus Time, showing periods when selected wells were active during history. (For interpretation of the references to colour in this figure legend, the reader is referred to the Web version of this article.)

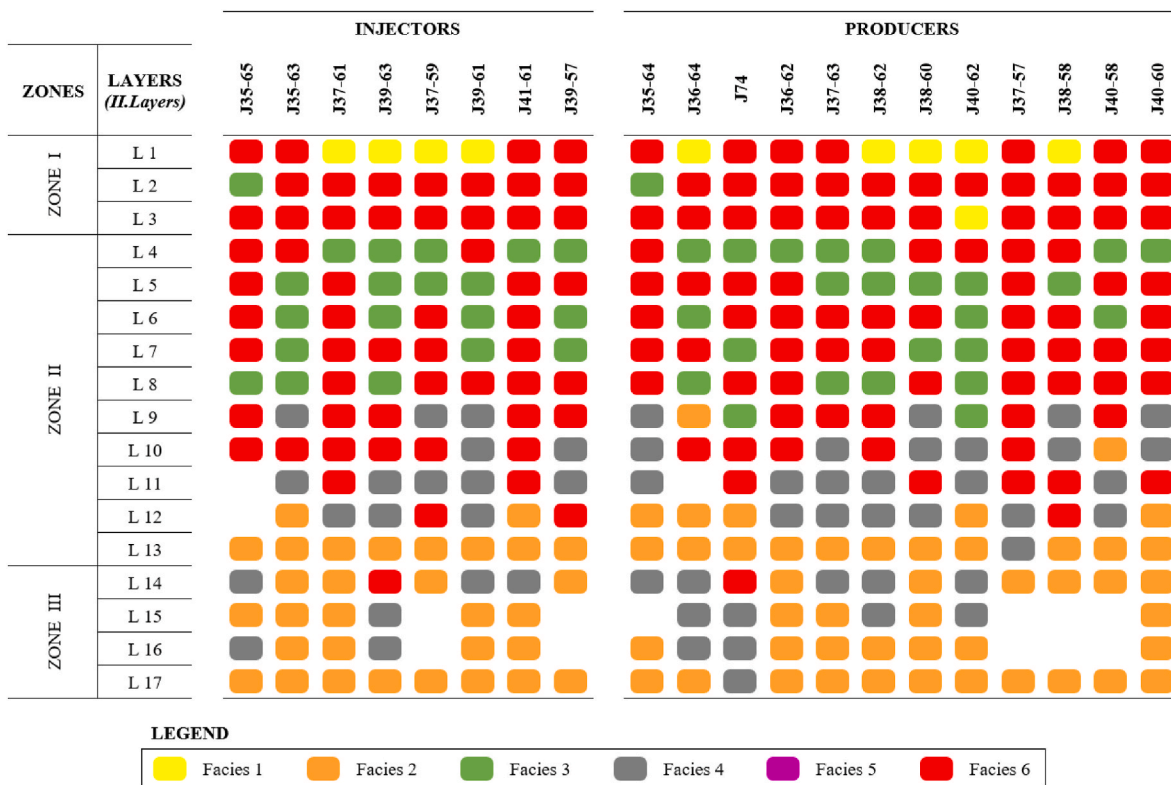


Fig. 13. Collation of Facies at selected wells used for characterizing Fault “A” in FEOF.

producer, while J37-67I represents well J37-67 when it was an injector. Using two wells to represent a producer that was later converted to an injector, was necessary to capture possible interactions between other injectors and such producers before they were converted to injectors. Two wells (J39-69 and XS95) were included as injectors (J39-69I and XS95I respectively) to evaluate possible well interactions with other wells around Fault “B”. However, the corresponding producer wells (J39-69P and XS95P) were excluded because of low cumulative liquid production. In summary, 22 wells were selected comprising 3 injectors and 9 producers west of Fault “B”, as well as 3 injectors and 7 producers east of the fault.

Arbitrary String Numbers (ASN) were assigned to the selected wells, showing active periods of the wells during the history. The six injectors were allocated ASNs 1 to 6 while, 11 to 26 were assigned to the 16 producers. These ASN assignments are summarized in Fig. 15a, with blue indicating that the well is west of Fault “B” and red indicates wells east of the fault. A plot of ASN versus Time (in months) is presented in Fig. 15b, showing months when the selected wells were active during the history. Historical injection and production data of the selected wells spanned 299 months, resulting in 299 data points. However, the wells were mostly active between the 24th month and the 252nd month, resulting

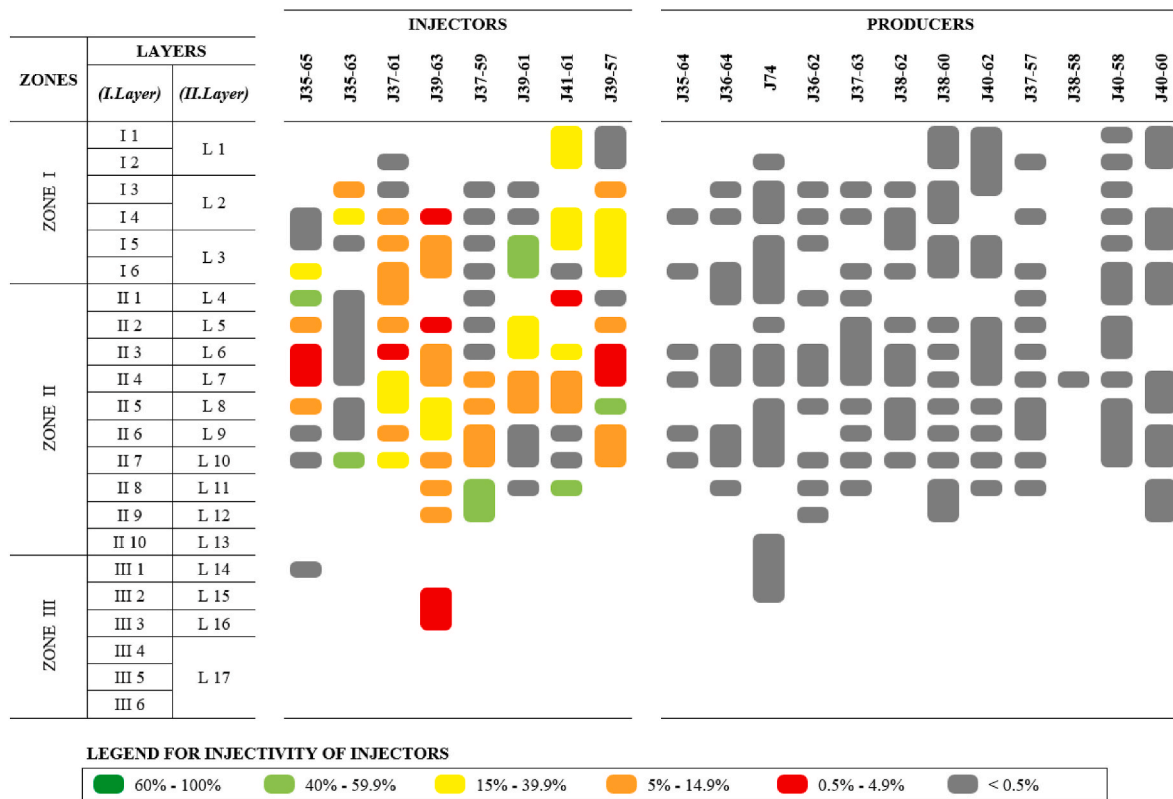


Fig. 14. Collation of Perforation Intervals at selected wells, with Injectivity of Injectors, using for characterizing Fault "A" in FEOF.

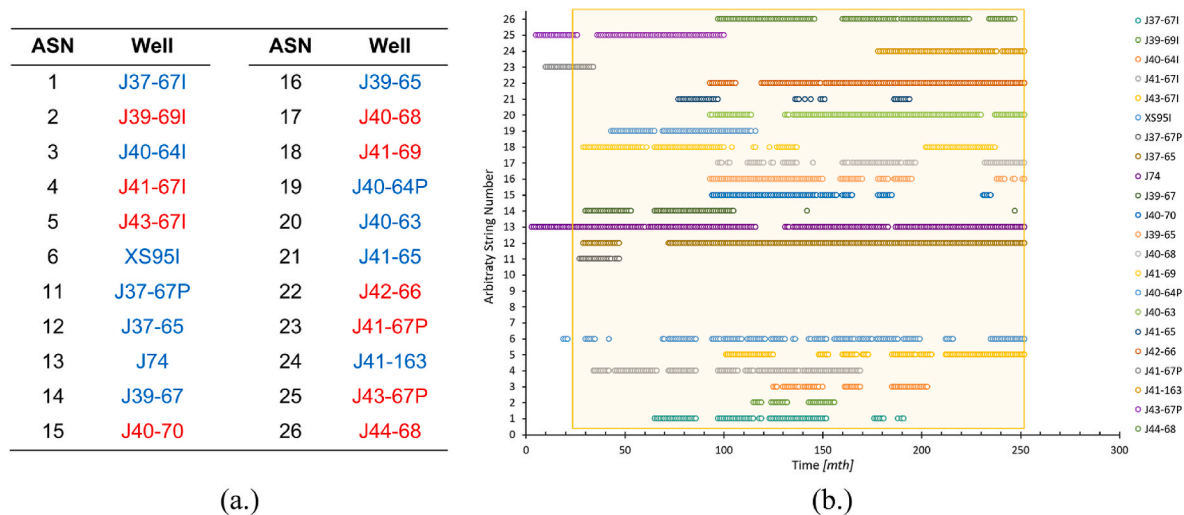


Fig. 15. (a.) Arbitrary String Numbers (ASN) assigned to selected Wells (blue wells are west of fault, red wells are east of fault); and (b.) Plot of ASN versus Time showing active periods of selected Wells around Fault "B". (For interpretation of the references to colour in this figure legend, the reader is referred to the Web version of this article.)

in 229 data points. The light-orange shaded portion of the plot represents this. This time window (24th month to 229th month) was chosen to capture possible interactions between producers (which were later converted to injectors) and other injectors. Also, the number of data points is greater than 208, which is the number of CRM parameters to optimize using only Production and Injection Terms.

Using the Facies Map of FEOF (see Fig. 7), the facies of the selected wells in each of the 17 layers (*II.Layer* nomenclature) were collated, and are presented in Fig. 16. Using this incorporates geology of FEOF in characterization of Fault "B". It is also important to note that the

indicated facies in each layer of the selected wells in Fig. 16 is not indicative of facies in between the wells. Data on perforation intervals of the selected wells (injectors and producers) and results from injectivity tests on injectors, which are based on the *I.Layer* nomenclature, were collated and presented in Fig. 17. The reported injectivity of injectors are colour-coded in Fig. 17. The CRM was calibrated using historical injection and production data. The resulting CRM parameters were thereafter combined with diagnostic plots, geologic data (summarized facies model) and wells data (perforation and injectivity data of wells) to characterize Fault "B" and identify other flow barriers.

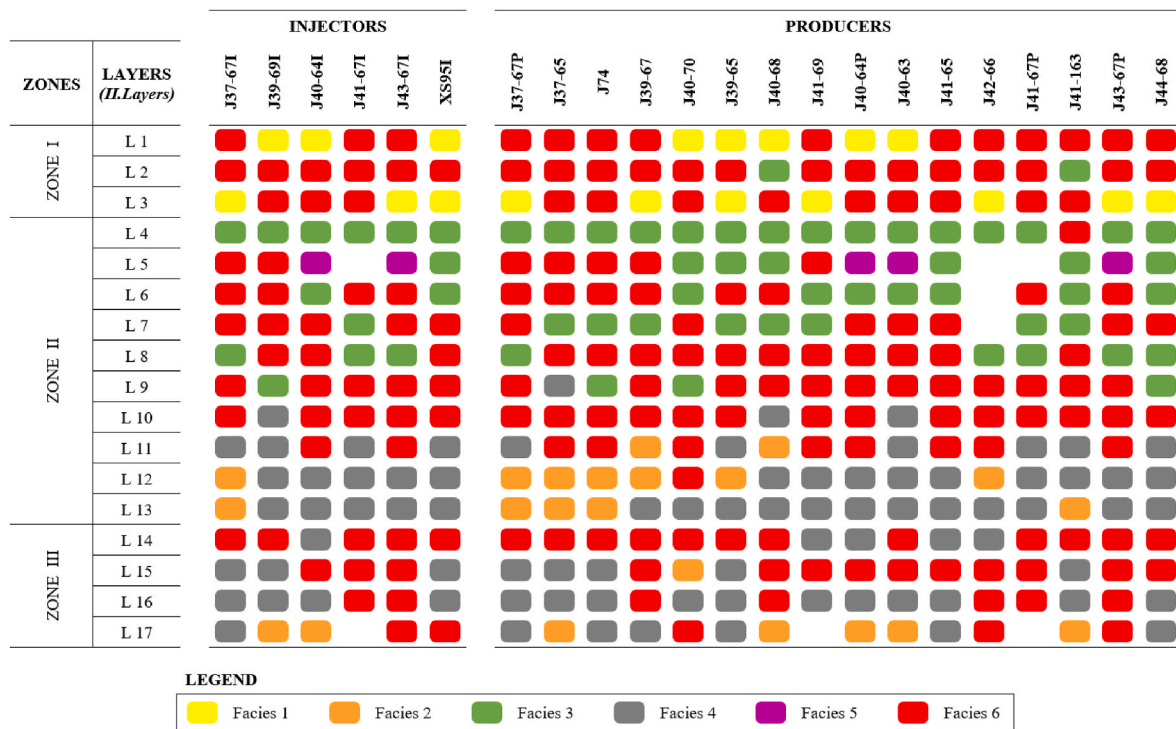


Fig. 16. Collation of Facies at selected wells used for characterizing Fault "B" in FEOF.

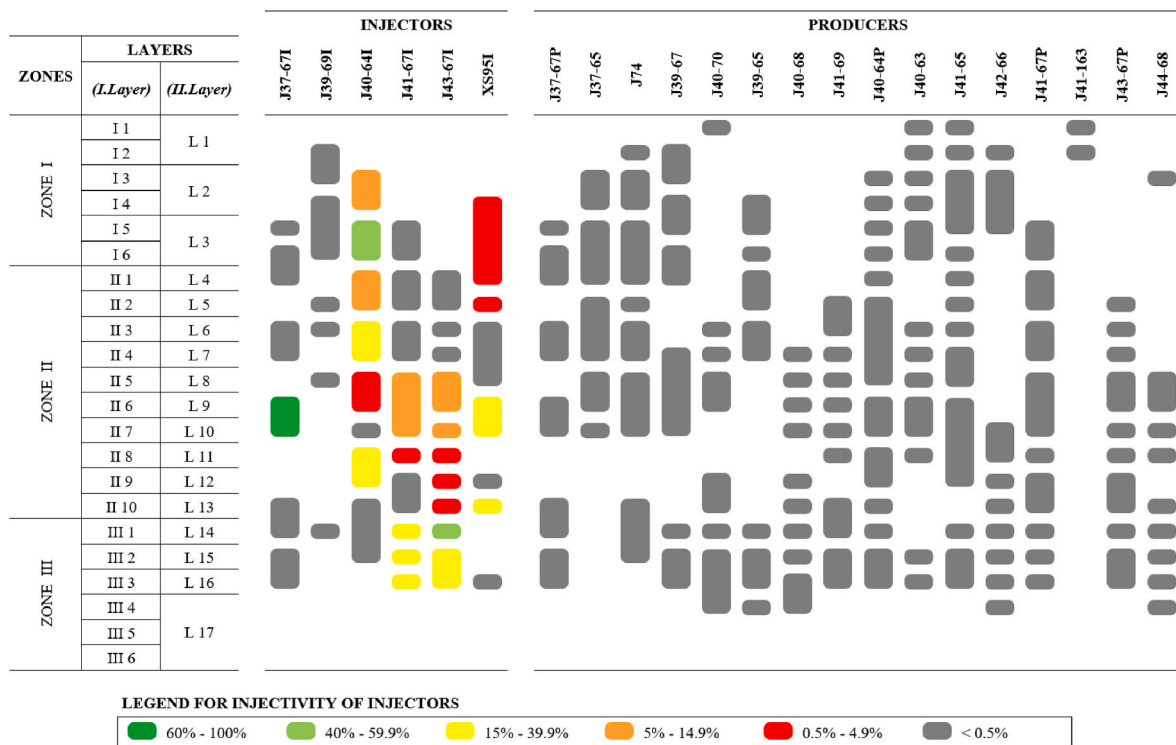


Fig. 17. Collation of Perforation Intervals at selected wells, with Injectivity of Injectors, using for characterizing Fault "B" in FEOF.

CASE A		CASE B				CASE C							
	P-01	P-02	P-03	P-04	P-01	P-02	P-03	P-04	P-01	P-02	P-03	P-04	
λ_{ij}	I-01	0.331	0.330	0.170	0.169	0.957	0.025	0.004	0.004	0.001	0.627	0.000	0.372
	I-02	0.330	0.172	0.329	0.169	0.484	0.017	0.186	0.305	0.493	0.006	0.495	0.006
	I-03	0.250	0.249	0.251	0.250	0.048	0.019	0.014	0.917	0.006	0.497	0.005	0.491
	I-04	0.170	0.327	0.170	0.332	0.167	0.154	0.003	0.671	0.005	0.498	0.000	0.497
	I-05	0.169	0.170	0.330	0.331	0.146	0.013	0.165	0.674	0.326	0.002	0.665	0.007
τ_{ij} [MTH]	P-01	P-02	P-03	P-04	P-01	P-02	P-03	P-04	P-01	P-02	P-03	P-04	
	I-01	0.600	0.600	0.772	0.759	0.602	6.983	9.474	4.451	4.983	0.741	7.550	0.948
	I-02	0.650	0.883	0.600	0.808	3.221	6.989	3.415	4.464	0.615	9.777	0.659	6.591
	I-03	0.619	0.641	0.622	0.610	7.089	6.985	9.469	0.794	5.013	0.698	7.546	0.719
	I-04	0.784	0.601	0.755	0.605	7.083	3.288	9.479	2.943	4.971	0.706	7.582	0.689
I-05	0.779	0.768	0.622	0.617	7.093	6.987	3.131	2.937	0.837	9.793	0.718	6.682	

Fig. 18. Optimized connectivity indices and time constants for all synfield cases.

14. Results

The CRM and Diagnostic Plots were validated using three synfield cases. These results are presented first. Thereafter, results from characterizing selected faults and identifying flow barriers in a real field are presented. This involved combining both tools with geological data and well data. Finally, the resulting structure map of the real field after fault characterization is presented.

15. Validation of CRM and diagnostic plots using synfield cases

Three synfield cases (Cases A, B and C) were used to validate CRM and the Diagnostic Plots. In Case A, the correlation coefficient for each producer was 0.9998. The producer time constants (in months) for P-01, P-02, P-03 and P-04 were 0.657, 0.784, 0.604 and 0.677 respectively. The injector-producer connectivity indices (λ_{ij}) and time constants (τ_{ij}) for Case A are summarized in Fig. 18. For each injector, the sum of all λ_{ij} 's was equal to 1.00, meaning that all the injected fluid was accounted for. The λ_{ij} 's of all injector-producer well-pairs essentially have one of three values: (i.) about 0.33 for close well-pairs of corner injectors; (ii.) about 0.17 for distant well-pairs of corner injectors; and (iii.) about 0.25 for the center injector, I-03, that communicates "equally" with all producers. Thus, well-pair distances affect the connectivity between injectors and producers.

Variations in τ_{ij} 's are also influenced by well-pair distances: about 0.6 month for close well-pairs compared to about 0.8 month for distant

well-pairs of corner injectors. With increasing well-pair distances, λ_{ij} 's decrease while τ_{ij} 's increase, showing an inverse relationship between λ_{ij} 's and τ_{ij} 's. The λ_{ij} 's and τ_{ij} 's are therefore independent of injection rates of injectors but are affected by well-pair distances. The Dynamic Flow Capacity (dFC) Plots and Flow Storage Index (I_{FS}) Plots for all producers are presented in Fig. 19. For each producer, the dFC curve deviates slightly from the 45-degree "homogeneity" line. This essentially indicates that the synfield in question is homogeneous, with symmetrical interactions between injectors and producers. The I_{FS} Plots also show the "homogeneity" between well-pairs of each producer; all injector-producer well-pairs have I_{FS} of about 0.50. This means that for each producer, a fraction of flow capacity at the producer was caused by an equal fraction of storage capacity swept by the injector.

In Case B, the permeability was less than that of the base case (Case A), and two high-permeability fractures exist; one between I-01 and P-01 and one between I-03 and P-04 (see Fig. 4). Injector-producer connectivity indices and time constants are summarized in Fig. 18. Due to the high-permeability fractures, well-pairs of I-01 and P-01, as well as I-03 and P-04 have the highest connectivity indices ($\lambda_{ij} > 0.9$). This was because, nearly all the injected fluid in I-01 and I-03 influence production rates of P-01 and P-04 respectively. Consequently, there was essentially no communication between I-01 and distant producers P-03 and P-04. There was little communication between I-03 and other producers (P-02, P-03 and P-04) because, all producers were equidistant from the injector.

The dFC and I_{FS} Plots for Case B are presented in Fig. 20. In producers

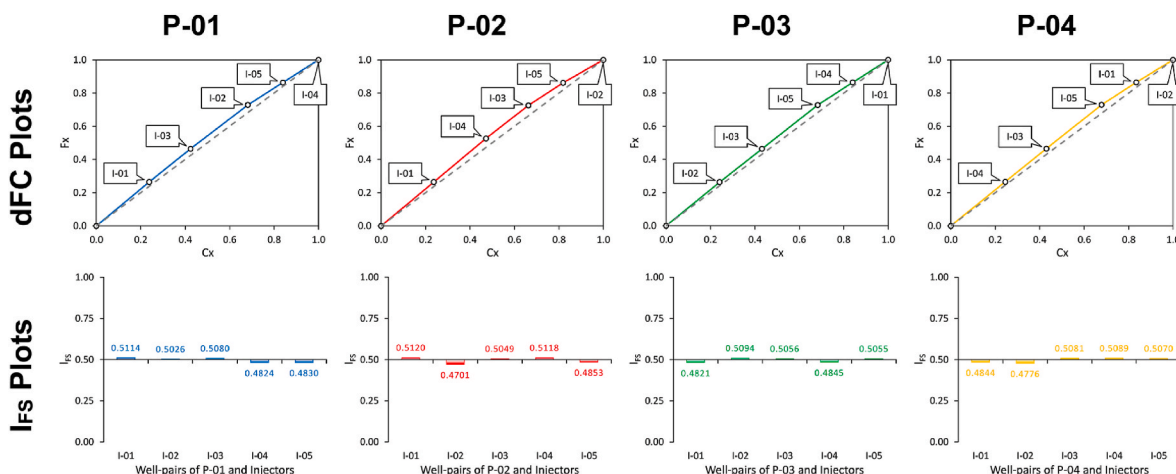


Fig. 19. Dynamic flow capacity (dFC) plots and flow storage index (I_{FS}) plots for all producers in Case A (Base Case).

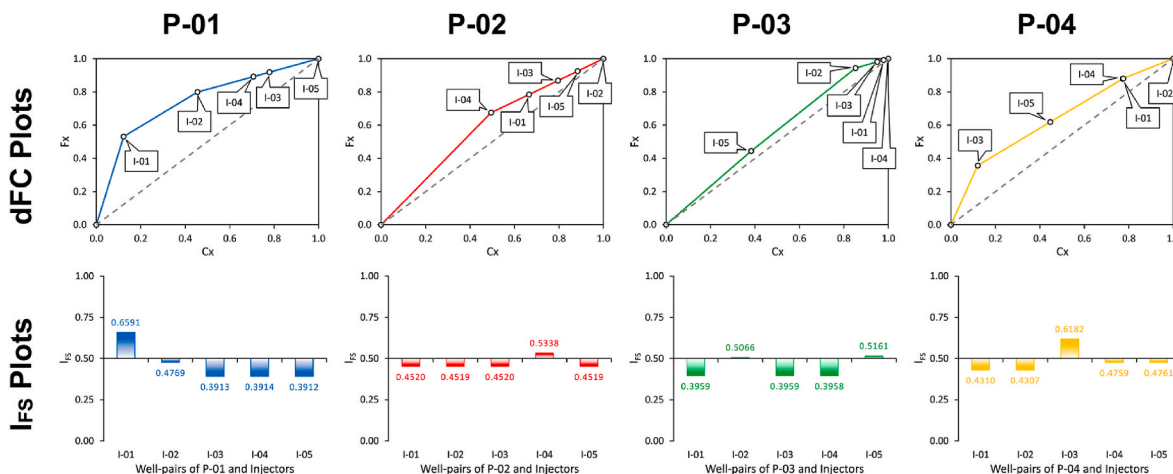


Fig. 20. Dynamic flow capacity (dFC) plots and flow storage index (I_{FS}) plots for all producers in Case B.

P-01 and P-04, there were substantial deviations between the dFC line and the 45-degree line. This was due to the high-permeability fractures between I-01 and P-01 well-pair of P-01, and I-03 and P-04 well-pair of P-04. There were smaller deviations of the dFC lines for producer P-02 and P-03 because, interactions between these producers and surrounding injectors were not via any fractures. However, these interactions were affected by the well-pair interactions via fractures, as shown in the I_{FS} Plots.

For P-03, injectors I-01 and I-03 had I_{FS} less than 0.40 showing impaired communication, which was due to fractures between these injectors and other producers (P-01 and P-04 respectively). There were no fractures between injector I-04 and any producers. However, there was impaired communication between I-04 and P-03. This was due to the strong communication between I-03 and P-04 via a high-permeability fracture. The I_{FS} Plots also show that, for the same well-pair distance, the interaction between I-01 and P-01 ($I_{FS} = 0.6591$) is stronger than that of I-03 and P-04 ($I_{FS} = 0.6182$), meaning that the 1000 mD fracture between I-01 and P-01 caused stronger communication than the 500 mD fracture between I-03 and P-04. Both diagnostic plots can be used to identify geological conditions in the synfield, with the I_{FS} Plot showing more details about such conditions.

A sealing fault divides the synfield into two separate compartments in Case C (see Fig. 4). There were essentially zero connectivity indices between well-pairs on either sides of the sealing fault (Fig. 18). These were well-pairs involving: (i.) producers P-01 and P-03 and injectors I-01, I-03 and I-04; and (ii.) producers P-02 and P-04 and injectors I-02

and I-05. The time constants are substantially higher for non-communicating well-pairs. For well-pairs in the same compartment, there are strong connectivity indices ($\lambda_{ij} > 0.2$) between the wells.

Dynamic Flow Capacity (dFC) Plots and I_{FS} Plots for Case C are presented in Fig. 21. There are small deviations between dFC lines of P-01 and P-04, and the 45-degree line. The deviations of the dFC lines for P-02 and P-03 are similar to those in the Case A, except that the wells are not “evenly spread” along the dFC line in this case. This shows that, except for the sealing fault that divides the synfield, the synfield is homogeneous.

One of the limitations in using the dFC Plots to characterize a field is the clustering of well-pairs on the dFC line, due to certain geological conditions. This is exemplified in Fig. 21, especially for producer P-03. The I_{FS} Plot overcomes this limitation. A quick glance of the I_{FS} Plots reveals the well-pairs on either side of the sealing fault. The values of I_{FS} within the same compartment indicate that the synfield is homogeneous ($I_{FS} \approx 0.50$). Both diagnostic plots identify geological conditions in a field of interest but the I_{FS} Plot is precise.

16. Characterization of fault “a” and flow barrier detection in EEOF

Using historical injection and production data from the selected wells around Fault “A”, the CRM was calibrated. Using the calibrated CRM, liquid production rates of the selected wells were generated. The observed liquid production rates and CRM-generated rates for each of

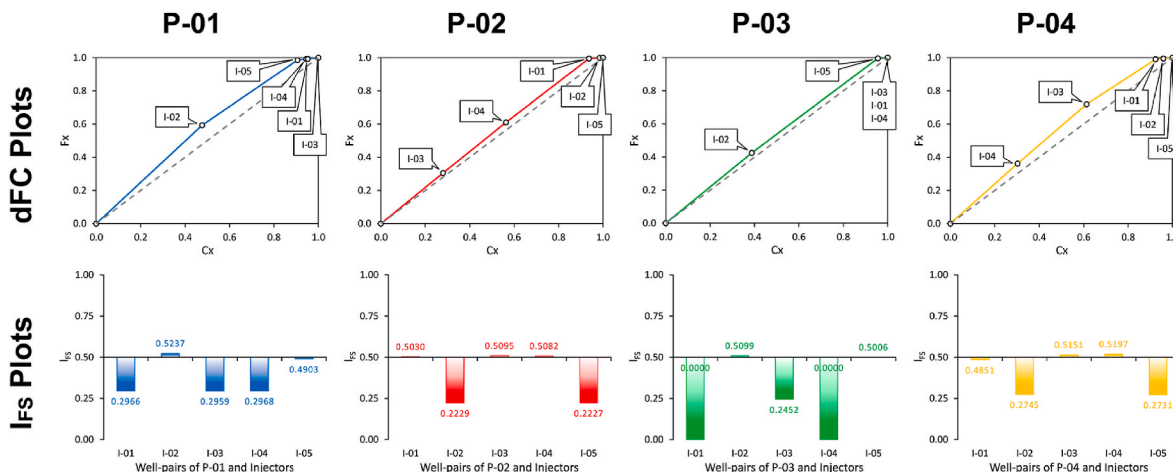


Fig. 21. Dynamic flow capacity (dFC) plots and flow storage index (I_{FS}) plots for all producers in Case c.

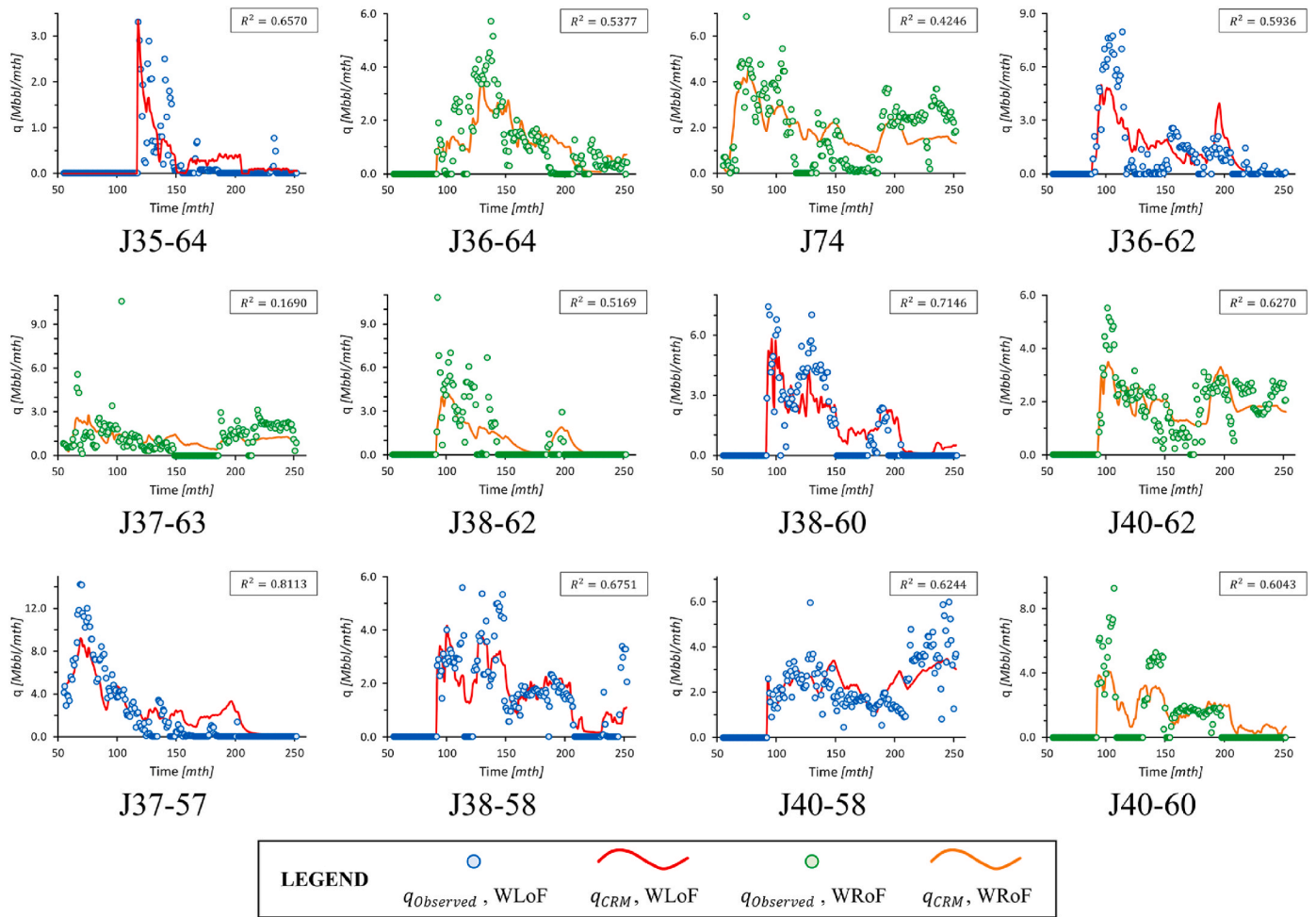


Fig. 22. Plots of Observed Production Rates ($q_{Observed}$) and CRM-generated Production Rates (q_{CRM}) for producers around Fault “A” in FEOF.

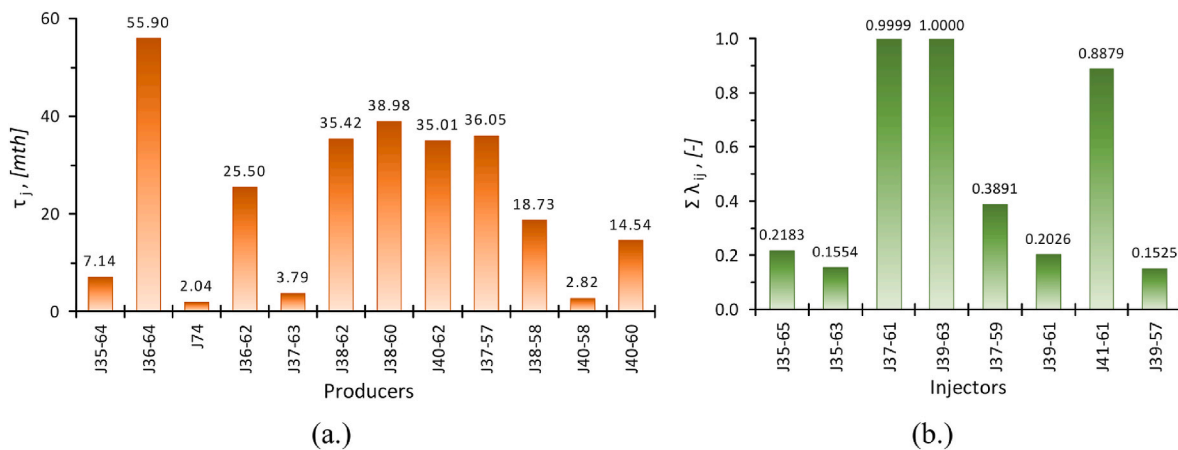


Fig. 23. (a.) Plots of Producer Time Constants (τ_{ij}); and (b.) Sum of Injector-Producer Connectivity Indices ($\sum \lambda_{ij}$) for each Injector, around Fault “A” in FEOF.

the selected producers, as well as the correlation coefficient (R^2) between these rates are presented in Fig. 22. The wells on either side of the fault were distinguished using “Well Left of Fault” (WLoF) and “Well Right of Fault” (WRoF).

Producer time constants (τ_{ij}), injector-producer connectivity indices (λ_{ij}) and injector-producer time constants (τ_{ij}) were the calibrated CRM parameters. Producer time constants and sum of λ_{ij} for each injector,

$\sum \lambda_{ij}$, are presented in Fig. 23. The $\sum \lambda_{ij}$ indicates the total fraction of injection water in each selected injector accounted for by the selected producers around the fault of interest. Based on the results from the CRM calibration, only two injectors (J37-61 and J39-63) had all their injected water accounted for.

The connectivity indices (λ_{ij}) of each injector-producer well-pair, and the τ_{ij} 's are presented in Fig. 24a and b respectively. The well names are

	J35-64	J36-64	J74	J36-62	J37-63	J38-62	J38-60	J40-62	J37-57	J38-58	J40-58	J40-60
J35-65	0.000	0.217	0.000	0.000	0.000	0.000	0.000	0.000	0.000	0.000	0.000	0.000
J35-63	0.000	0.000	0.065	0.000	0.000	0.000	0.000	0.090	0.000	0.000	0.000	0.000
J37-61	0.000	0.001	0.068	0.287	0.030	0.235	0.108	0.155	0.116	0.000	0.000	0.000
J39-63	0.000	0.000	0.000	0.106	0.000	0.000	0.000	0.739	0.143	0.011	0.000	0.000
J37-59	0.029	0.000	0.046	0.000	0.060	0.000	0.035	0.000	0.000	0.089	0.000	0.130
J39-61	0.000	0.071	0.000	0.000	0.000	0.000	0.064	0.000	0.000	0.067	0.000	0.000
J41-61	0.011	0.000	0.168	0.000	0.123	0.000	0.000	0.092	0.016	0.022	0.419	0.037
J39-57	0.000	0.027	0.000	0.000	0.000	0.000	0.008	0.000	0.000	0.059	0.000	0.058

(a.)

	J35-64	J36-64	J74	J36-62	J37-63	J38-62	J38-60	J40-62	J37-57	J38-58	J40-58	J40-60
J35-65	48.27	6.20	68.91	67.58	79.73	49.62	48.83	4.76	0.04	76.75	37.71	15.20
J35-63	0.05	19.85	11.23	29.58	57.64	0.04	63.09	0.08	1.80	2.99	50.71	0.04
J37-61	0.04	40.70	4.01	5.80	1.04	6.15	0.03	2.93	3.42	0.04	0.04	2.94
J39-63	0.03	42.71	0.03	0.96	20.84	0.04	63.40	307.37	10.18	0.03	70.22	0.03
J37-59	0.14	0.04	165.71	49.23	133.62	42.78	0.03	95.25	4.68	0.55	44.93	3.37
J39-61	17.02	3.39	128.00	64.80	0.04	336.61	1.83	37.46	0.06	5.83	69.99	31.20
J41-61	0.04	0.03	12.25	38.15	11.73	4.50	0.03	9.13	6.53	12.86	19.47	0.03
J39-57	55.35	0.09	38.06	0.04	0.63	0.04	0.04	99.38	69.21	0.53	58.82	2.71

(b.)

Fig. 24. (a.) Connectivity Indices and (b.) Time Constants (in months) for Injector-Producer Well-Pairs around Fault “A” in FEOF.

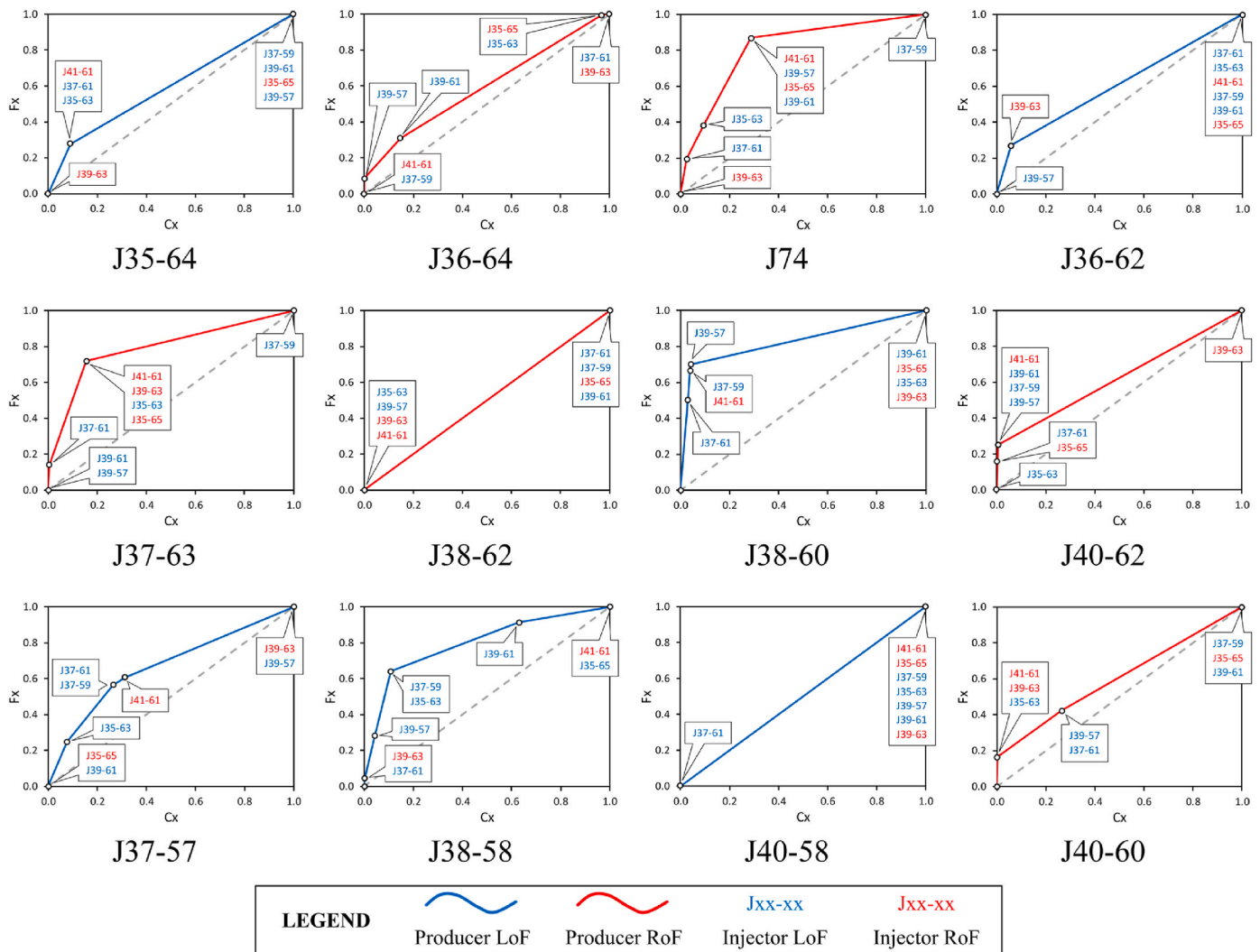


Fig. 25. Dynamic Flow Capacity (dFC) Plots of selected producers and injectors around Fault “A” in FEOF.

colour-coded: wells left of the fault are indicated in blue; red indicates wells right of the fault. Only well-pairs with $\lambda_{ij} \approx 0.0$ and their corresponding τ_{ij} 's are shaded. There are 36 well-pairs with non-zero λ_{ij} 's. Using these CRM parameters, the Dynamic Flow Capacity (dFC) Plots and Flow Storage Index (I_{FS}) Plots were developed, and are presented in Figs. 25 and 26 respectively. Colour coding was also used to distinguish between wells left of the fault (LoF) and wells right of the fault (RoF). Presenting both dFC and I_{FS} plots was necessary to showcase improvements in interwell communication assessment using I_{FS} plots.

16.1. Producer J35-64

There appears to be connectivity between J35-64 and two injectors: J37-59 and J41-61 (Fig. 24a). No communication between J35-64 and other injectors is clearly shown in Figs. 24a and 26. On the dFC plot, these well-pairs were clustered, which may or may not indicate lack of communication. In the I_{FS} plot however, it is clear that there is no communication between J35-64 which is left of Fault “A” and two injectors right of the fault: J35-65 (a nearby well) and J39-63. This is despite some facie continuity and similarity in perforation intervals (see

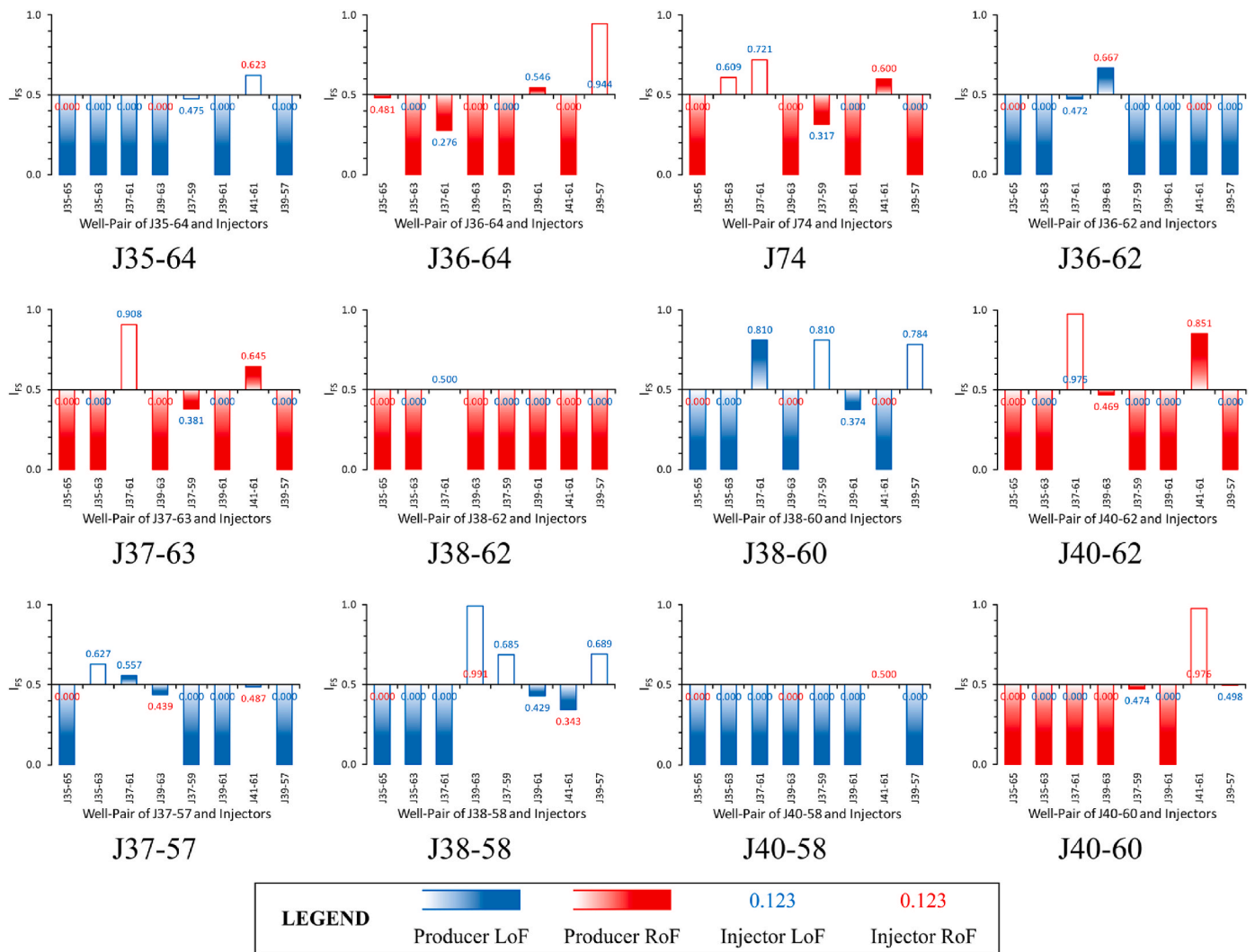


Fig. 26. Flow Storage Index (I_{Fs}) Plots of selected producers and injectors around Fault “A” in FEOF.

Figs. 13 and 14 respectively) between J35–64 and J35-65, meaning that the section of Fault “A” near J35-64 is sealing. Using the complete facie map (2 layers are shown in Fig. 7b and c), the zero connectivity between J35–64 and J39-63 is likely due to facie discontinuity.

The insignificant connectivity between J35-64 and injector J41-61 is essentially a false positive since the τ_{ij} is 0.04 month (about 1 day) because, a well-pair with that τ_{ij} will likely have a much higher λ_{ij} , especially considering the relative distance between these wells. Despite sand facie continuity in two layers, this is likely due to several factors: (i.) possible sealing section of Fault “A” near J35-64; (ii.) possible interwell interactions in between this well-pair; and (iii.) the relative distance of this well-pair. Consequently, the bar for this well in Fig. 26 is not shaded. Negligible communication between J35-64 and injector J37-59, both left of the fault, is likely also a false positive considering: (i.) the τ_{ij} of the well-pair (Fig. 24b); (ii.) the relative distance between the wells (see Fig. 11); and (iii.) the sand facie discontinuity between these wells (see Fig. 7).

16.2. Producer J36-64

Zero communication between J36-64 and injector J35-63 means that the section of Fault “A” near J36-64 is sealing (see Figs. 24 and 26); a deduction not apparent with only Fig. 25 because of the cluster of well-pairs. This is corroborated by fault throw of about 15 m in between this well-pair, and facie thickness less than 3 m in more than 75% of the

layers. There is strong connectivity between J36-64 and injector J35-65, both right of the fault. With negligible connectivity and limited sand facie continuity between the well-pair of J36-64 and injector J39-61, there may be some communication across some sections of Fault “A”. The lack of communication between J36-64 and two injectors (J39–63 and J41-61), despite some similarities in perforation intervals (see Fig. 14), is likely largely due to sand facie discontinuity in most layers and other well-pair interactions between these well-pairs.

In spite of the “non-zero” λ_{ij} , there is essentially no communication between J36–64 and J37-61 (see Figs. 24–26). This is either due to other well-pair interactions between this well-pair and/or no communication across sections of the fault in between this well-pair. Considering that $\tau_{ij} = 0.09$ month (about 3 days) and the relative well-pair distance, the negligible connectivity between J36–64 and J39-57 is a false positive. No connectivity exists between J36-64 and injector J37-59.

16.3. Producer J74

Despite limited sand facie continuity and similarities in perforation intervals (see Figs. 7, 13 and 14), there is no connectivity between J74 and injector J39-63. With substantial variations in sand facie thickness between these wells, this corroborates the possibility of facie discontinuity north of J39-63, as deduced from the well-pairs of producers J35–64 and J36-64 with injector J39-63. Zero connectivity between J74 and injector J35-65 is likely due to other well-pair interactions in

between this well-pair. No communication between J74 and injectors J39-61 and J39-57 that are left of the fault, means that several sections along Fault "A" are likely sealing.

In spite of substantial communication between J74 and injectors J35-63 and J37-61, as shown in Figs. 25 and 26, there is negligible connectivity between these well-pairs (Fig. 24). This negligible connectivity means that the section of Fault "A" just south of J36-64 is partially sealing. Based on dFC and I_{FS} plots, the negligible connectivity and large time constant between J74 and injector J37-59 is likely due to other well-pair interactions in between this well-pair. Despite limited sand facie continuity, there appears to be significant connectivity between J74 and injector J41-61.

16.4. Producer J36-62

Two injectors, J37-61 and J39-63, have non-zero connectivity indices with J36-62. The communication between J36-62 and J39-63 shows that the section of Fault "A" near J37-63 is likely partially sealing. Zero connectivity between J36-62 and injector J35-65 corroborates the deduced sealing section of Fault "A" near producers J35-64 and J36-64. Despite facie continuity and similarities in perforation intervals between J36-62 and injector J35-63, there is zero connectivity and communication (Figs. 24 and 26). There is the possibility of a sealing baffle between this well-pair. Lack of communication between J36-62 and injector J39-61 in spite of limited sand facie continuity is likely due to the strong connectivity between J36-62 and injector J37-61. Zero connectivity between J36-62 and injectors J37-59 and J39-57 even with some sand facie continuity and similar perforation intervals is likely due to other interwell interactions. Possible sealing sections along Fault "A" and facies discontinuities are likely the reason for zero connectivity between J36-62 and injector J41-61.

16.5. Producer J37-63

There is negligible communication between J37-63 and injector J37-61, meaning that the section of Fault "A" near J37-63 is partially sealing. This is corroborated by the significant connectivity between J36-62 and injector J39-63. Despite limited sand facie continuity (see Fig. 7), there is significant connectivity (Fig. 24) and high communication (Fig. 26) between J37-63 and injector J41-61, both right of Fault "A". The negligible connectivity (Fig. 24) and partial communication (Fig. 26) between J37-63 and J37-59 corroborates that the section of Fault "A" near J37-63 is partially sealing. The zero connectivity between J37-63 and injector J39-57 is due to: (i.) sand facie discontinuity; and (ii.) other interwell interactions between this well-pair. Zero connectivity between J37-63 and injector J39-61 is likely due to other well-pair interactions in between this well-pair, as well as sealing sections along Fault "A". Lack of communication between J37-63 and J39-63, despite facie continuity in several layers with corresponding facie thickness greater than 2 m, could mean that there is a sealing baffle between this well-pair. Despite sand facie continuity in few layers, the zero connectivity between J37-63 and J35-63 corroborates the flow barrier just north of J36-62 that extends close to Fault "A". Interactions between other well-pairs likely led to no communication between J37-63 and J35-65.

16.6. Producer J38-62

Zero connectivity between J38-62 and injector J35-63 is due to limited sand facie continuity and substantial facie thickness variation between this well-pair. Interactions between other wells likely led to zero connectivity between J38-62 and injector J35-65. The zero connectivity between J38-62 and injector J39-63, in spite of sand facie continuity in several layers with layer thickness greater than 2 m, means that there is likely a sealing baffle between this well-pair, which extends to in between producer J37-63 and injector J39-63. The strong

connectivity between J38-62 and injector J37-61 shows that the section of Fault "A" just west of J38-62 is not sealing. Zero connectivity indices between J38-62 and injectors J37-59 and J39-57, is likely due to limited sand facie continuity and other well interactions between the well-pair. Zero connectivity between J38-62 and injector J39-61 confirms that the section of Fault "A" near J39-61 is sealing. Limited sand facie continuity with substantial variation in thickness, and other well-pair interactions likely led to the zero connectivity between J38-62 and injector J41-61.

The dFC plot depicts equal flow capacity per storage capacity (or "homogeneity") between J38-62 and injector J37-61 (Fig. 25). This is also depicted in the I_{FS} plot, with $I_{FS} = 0.500$ (Fig. 26). This occurred because, this producer has non-zero connectivity index with only one of the selected injectors. These depictions of "homogeneity" from these diagnostic plots shows that they are better suited for multi-well interactions with a selected producer or injector, but not for one well-pair.

16.7. Producer J38-60

The significant connectivity between J38-60 and injector J37-61 is likely a false positive, considering that the τ_{ij} of this well-pair is 0.03 month (Fig. 24b). However, ample sand facie continuity in several layers with layer thickness greater than 1.5 m, and the relative distance between this well-pair make the "false positive" inference questionable. Therefore, there is likely high (not necessarily extreme) communication between this well-pair (see Figs. 3 and 26). The negligible connectivity between J38-60 and injector J37-59 is questionable, considering that the τ_{ij} is 0.03 month. This however does not mean that there is no communication between these wells. The insignificant connectivity (Fig. 24) and extreme communication (Fig. 26) between the J38-60 and injector J39-57 is a false positive considering: (i.) the τ_{ij} is 0.04 month; (ii.) the sand facie discontinuities between the wells (see Fig. 7); (iii.) the relative distance between the wells; and (iii.) other interwell interactions in between this well-pair.

There is negligible connectivity between J38-60 and injector J39-61, both left of the fault. Despite some similarities in facies and perforation intervals at the wells (see Figs. 13 and 14), limited facie continuity and other interwell interactions led to zero connectivity between J38-60 and injector J35-63. Zero connectivity between J38-60 and injector J35-65 is likely due to several sealing sections of Fault "A" as well as interactions of other well-pairs in between this well-pair. The well-pairs of J38-60 and injectors J39-63 and J41-61 have sand facie continuity in few layers but zero connectivity, confirming the sealing section of Fault "A" near injector J39-61.

16.8. Producer J40-62

Significant connectivity between J40-62 and injector J37-61 confirms the "not sealing" section of Fault "A" near J38-62. Zero connectivity between J40-62 and two injectors (J39-61 and J37-59) left of Fault "A" confirms the sealing section of Fault "A" near J39-61. With essentially no facie continuity, several sealing sections of Fault "A" and the influences of other interwell interactions, the well-pair of J40-62 and injector J39-57 has zero connectivity. The negligible connectivity but extreme communication ($I_{FS} > 0.75$) between J40-62 and injector J41-61, both right of the fault, is questionable. A combination of strong connectivity and high time constant were obtained for the well-pair of J40-62 and injector J39-63, resulting in impaired communication as shown in Fig. 26. Zero connectivity indices between J40-62 and injectors J35-65 and J35-63 are due to: (i.) almost no sand facie continuity coupled with significant layer thickness variations; (ii.) other well-pair interactions; and (iii.) several sealing sections of Fault "A".

16.9. Producer J37-57

The zero connectivity between J37-57 and injector J35-65 are due to: (i.) almost no sand facie continuity between the wells; (ii.) other

interwell interactions; (iii.) the large well-pair distance; and (iv.) several sealing sections along Fault “A”. Negligible and substantial connectivities between J37-57 and injectors J35-63 and J37-61 respectively, are due to sand facie continuity in several layers between these wells. Interestingly, there is zero connectivity between J37-57 and injector J37-59, which is likely due to other interwell interactions (J36-58 and J37-59). Despite sand facie continuity in few layers between J37-57 and injector J39-63, the significant connectivity and impaired communication ($I_{FS} = 0.439$) of this well-pair is rather bizarre, considering several sealing sections of Fault “A” in between the well-pair.

Zero connectivity between J37-57 and injector J39-57 is likely due to other interwell interactions and possible fluid property variations, considering the sand facie continuity in several layers (see Figs. 7 and 13) as well as similar perforation intervals (see Fig. 14) between this well-pair. There is insignificant connectivity between J37-57 and injector J41-61 that is east of Fault “A”. This means that there is some communication across the section of the fault in between these well-pairs. The zero connectivity between J37-57 and injector J39-61 is likely due to the negligible connectivity between J38-58 and J39-61. This is because, J38-58 is in between J37-57 and J39-61, thereby possibly hindering communication between these wells.

16.10. Producer J38-58

Negligible connectivity between J38-58 and injector J41-61 confirms the deduced communication across the section of the fault in between injector J41-61 and producers J37-57 and J38-58. This section is likely partially sealing. The well-pair of J38-58 and injector J39-61 have negligible connectivity and impaired communication (see Figs. 25 and 26). The insignificant connectivity between J38-58 and injector J39-63 is a false positive, since $\tau_{ij} = 0.03$ month (about 1 day), and corroborates the questionable significant connectivity between J37-57 and J39-63. Negligible connectivities exist between J38-58 and injectors J37-59 and J39-57 with τ_{ij} 's of 0.55 month and 0.53 month respectively, thereby resulting in seemingly high communication between these well-pairs (see Figs. 25 and 26). These connectivities are therefore questionable. Zero connectivity and communication between J38-58 and two relatively distant injectors (J35-63 and J35-65) is due to: (i.) other interwell interactions; (ii.) sand facies discontinuity; (iii.) several sealing sections of Fault “A”. This also confirms the sealing baffle south of J35-63. Considering sand facie continuity in several layers, interwell communication between other well-pairs likely led to the zero connectivity between J38-58 and injector J37-61.

16.11. Producer J40-58

Limited facie continuity, substantial thickness variations and other interwell interactions likely caused the zero communication between J40-58 and injector J39-61. Strong connectivity exists between J40-58 and injector J41-61, showing that there is communication across the section of Fault “A” in between these wells. However, the τ_{ij} is high (19.47 months) for that connectivity index, which confirms that that section is partially sealing. There is no communication between J40-58 and several injectors: J35-65, J35-63, J37-61 and J39-63. This is due to: (i.) several sealing sections along Fault “A”; (ii.) interactions of other well-pairs; and (iii.) the sealing baffle south of J35-63. With sand facie continuity in few layers and similar perforation intervals, the zero connectivity between J40-58 and injectors J37-59 and J39-57 is likely due to other interwell communications, such as the negligible connectivity between J38-58 and J37-59 with relatively shorter well-pair distance. The strong connectivity between J40-58 and injector J41-61 corroborates the partial sealing inference of the section of Fault “A” in between this well-pair.

Similar to the observation in producer J38-62, J40-58 has non-zero connectivity with only one injector, J41-61. The dFC plot therefore depicts equal flow capacity per storage capacity (or “homogeneity”)

between this well pair (Fig. 25). Also, the $I_{FS} = 0.500$ for this well-pair (Fig. 26). This therefore confirms that these diagnostic plots are better suited for multi-well interactions with a selected producer or injector, but not for one well-pair.

16.12. Producer J40-60

Besides the well-pair of J40-60 and injector J41-61 having $\tau_{ij} = 0.03$ month with negligible connectivity ($\lambda_{ij} = 0.037$), the well-pair also appears to have an infinite conductivity path as shown in Figs. 25 and 26, which is clearly contradictory. Thus, this connectivity is a false positive. Zero communication between J40-60 and injector J39-61 confirms the sealing section of Fault “A” near J39-61. This sealing section is also corroborated by the zero communication between J40-60 and injector J37-61. Limited sand facie continuity and other interwell interactions led to the zero connectivity between J40-60 and injector J39-63. Several sealing sections along Fault “A”, other well-pair interactions and the sealing baffle south of J35-63, led to zero connectivity between J40-60 and injectors J35-65 and J35-63. Substantial and negligible connectivities between J40-60 and injectors J37-59 and J39-57 respectively, indicate that the section of the fault west of J40-60 is partially sealing. This is also confirmed by the interactions between injector J41-61 and three producers left of the fault: J40-58, J37-57 and J38-58.

17. Characterization of fault “B” and flow barrier detection in FEOF

The CRM was also calibrated using historical injection and production data from selected faults around Fault “B” in the Far East Oil Field (FEOF). Thereafter, the calibrated CRM was used to generate liquid production rates of the selected producers. Comparison between observed liquid production rates and CRM-generated liquid production rates, as well as the respective correlation coefficients (R^2) between these rates, are presented in Fig. 27. The wells on either side of the fault were distinguished using “Well Left of Fault” (WLoF) and “Well Right of Fault” (WRoF).

Calibrated CRM parameters were producer time constants (τ_j), injector-producer connectivity indices (λ_{ij}) and injector-producer time constants (τ_{ij}). The producer time constants and sum of λ_{ij} for each injector, $\sum \lambda_{ij}$, are presented in Fig. 28. Based on the results from the CRM calibration, only one injector (XS95I) had nearly all its injected water accounted for, while injector J39-69I essentially did not influence any of the selected producers.

The λ_{ij} 's and τ_{ij} 's of each injector-producer well-pair are presented in Fig. 29a and b respectively. The well names are colour-coded: wells left of the fault are indicated in blue; red indicates wells right of the fault. Only well-pairs with $\lambda_{ij} \approx 0.0$ and their corresponding τ_{ij} 's are shaded. There are 40 well-pairs with non-zero λ_{ij} 's. Using these CRM parameters, the Dynamic Flow Capacity (dFC) Plots and Flow Storage Index (I_{FS}) Plots were developed, and are presented in Figs. 30 and 31 respectively. Using colour-coding, wells left of the fault (LoF) were distinguished from those right of the fault (RoF). The dFC and I_{FS} plots were both presented to showcase improvements in interwell communication assessment using I_{FS} plots.

17.1. Producer J37-67P

There is zero connectivity between J37-67P and injector J37-67I (Fig. 29a). This is expected since both wells are actually J37-67 operated as producer and injector respectively. The insignificant connectivity between J37-67P and injector J41-67I (which is right of the fault) is likely a false positive since this $\tau_{ij} = 0.14$ month (Fig. 29b) for this well-pair. Zero communication between J37-67P and injector XS95I (both left of the fault) is likely due to other interwell interactions and limited sand facie continuity between this well-pair. Although J37-67P has zero connectivity with other injectors (J39-69I, J40-64I and J43-

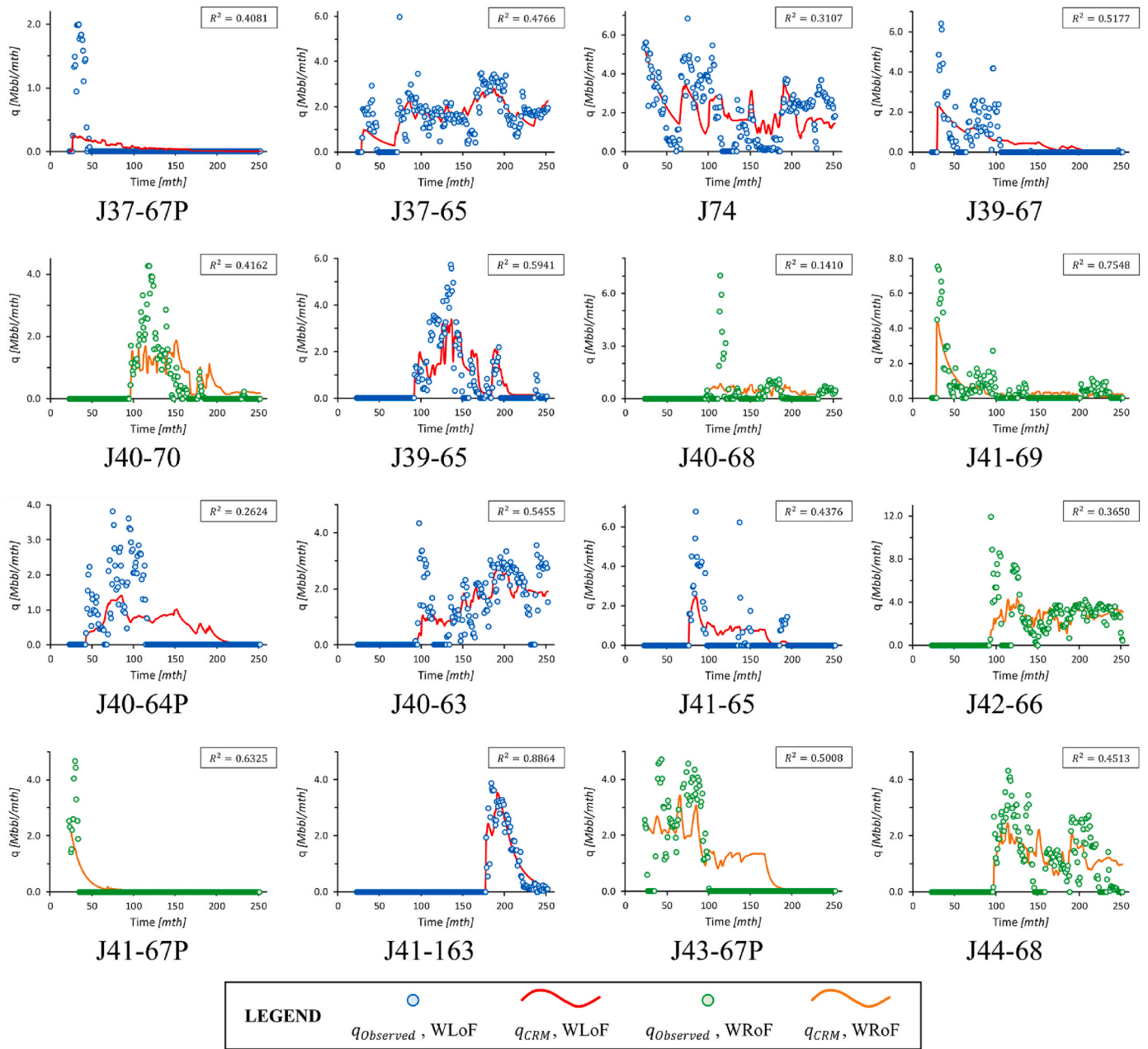


Fig. 27. Plots of Observed Production Rates ($q_{observed}$) and CRM-generated Production Rates (q_{CRM}) for producers around Fault “B” in FEOF.

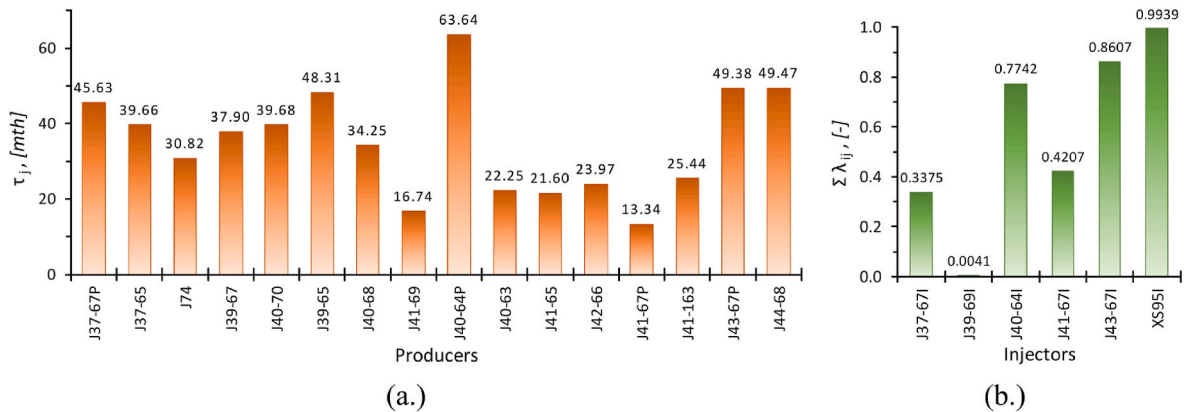


Fig. 28. (a.) Plots of Producer Time Constants (τ_j); and (b.) Sum of Injector-Producer Connectivity Indices ($\sum \lambda_{ij}$) for each Injector, around Fault “B” in FEOF.

	J37-67P	J37-65	J74	J39-67	J40-70	J39-65	J40-68	J41-69	J40-64P	J40-63	J41-65	J42-66	J41-67P	J41-163	J43-67P	J44-68
(a.) J37-67I	0.000	0.000	0.129	0.036	0.081	0.000	0.028	0.011	0.052	0.000	0.000	0.000	0.000	0.346	0.000	0.082
J39-69I	0.000	0.000	0.000	0.000	0.000	0.004	0.000	0.000	0.000	0.000	0.000	0.000	0.000	0.002	0.000	0.000
J40-64I	0.000	0.000	0.000	0.000	0.000	0.196	0.000	0.000	0.000	0.560	0.018	0.000	0.000	0.226	0.000	0.000
J41-67I	0.002	0.000	0.000	0.000	0.073	0.098	0.000	0.000	0.044	0.009	0.074	0.120	0.000	0.080	0.128	0.052
J43-67I	0.000	0.244	0.128	0.000	0.027	0.010	0.031	0.011	0.000	0.058	0.000	0.352	0.000	0.000	0.000	0.139
XS95I	0.000	0.320	0.258	0.000	0.000	0.000	0.030	0.026	0.000	0.262	0.000	0.098	0.006	0.000	0.000	0.000
(b.) J37-67I	25.76	95.73	5.33	11.24	4.48	39.20	4.64	14.59	9.02	123.72	49.26	69.61	24.77	18.42	20.83	3.65
J39-69I	35.00	88.43	124.56	83.32	6.39	0.09	36.34	75.17	83.04	23.21	90.24	58.92	30.89	10.58	93.74	8.75
J40-64I	34.92	77.31	2.67	82.07	10.96	1.38	46.37	50.94	86.38	196.88	1.48	118.98	33.23	11.42	91.35	6.78
J41-67I	0.14	66.26	41.78	46.23	0.04	1.77	8.57	29.75	14.28	0.05	4.08	1.09	16.11	10.58	5.44	0.05
J43-67I	26.74	171.35	2.62	72.56	7.99	14.59	7.00	43.50	3.79	1.90	77.17	14.07	25.56	50.41	77.38	8.88
XS95I	5.18	15.60	294.73	16.49	42.80	7.30	0.11	0.93	2.15	60.69	5.84	0.07	0.11	11.42	5.93	40.37

Fig. 29. (a.) Connectivity Indices and (b.) Time Constants (in months) for Injector-Producer Well-Pairs around Fault “B” in FEOF.

67I), which could lead to several inferences, an examination of the active periods of these well-pairs during the entire history (see Fig. 15) reveals that the other injectors and J37–67P were not active during the same period, leading to zero connectivity between these well-pairs.

Equal flow capacity per storage capacity (or “homogeneity”) between J37–67P and J41-67I, is depicted by the dFC plot and I_{FS} plot ($I_{FS} = 0.500$), as shown in Figs. 30 and 31 respectively. This is because, this well-pair is the only well-pair with non-zero λ_{ij} for the selected wells. Thus, these diagnostic plots are better suited for evaluating multi-well interactions between a selected well and surrounding wells, not for one well-pair.

17.1.1. Producer J37-65

In spite of sand facie continuity in several layers and similarities in perforation intervals (see Figs. 7, 16 and 17), there is zero connectivity between J37–65 and J37-67I (Fig. 29). This is likely due to one of several possibilities: (i.) the interplay of fluid property variations between the well-pair; and (ii.) substantial thickness variations in at least 50% of the layers with sand facie continuity. Zero connectivity and no communication (Figs. 29–31) between J37-65 and injector J39-69I confirms that the section of Fault “B” between producers J37–67P and J37-65 (left of the fault) and injector J39-69I is sealing. Zero connectivity between J37-65 and injector J40-64I is likely due to limited sand facie continuity and other well-pair interactions, such as between producer J39–65 and J40-64I. Due to the zero communication between J37-65 and injector J41-67I, the section of Fault “B” near J41-67I is likely sealing.

There is strong connectivity between J37-65 and injector J43-67I. This is however contradicted with very high τ_{ij} (Fig. 29b) and impaired communication (Fig. 31). There is also strong connectivity between J37-65 and injector XS95I with relatively high τ_{ij} (for that connectivity index), which is depicted as communication via high-permeability streaks in dFC and I_{FS} plots (see Figs. 30 and 31 respectively). Considering sand facie discontinuities and the relative distances of these well-pairs, the inferred “strong connectivities” are therefore questionable, and depicted by empty bars in the I_{FS} plot.

17.1.2. Producer J74

There is significant connectivity between J74 and injector J37-67I, both left of Fault “B”. This is depicted, howbeit exaggerated, as strong communication in dFC and I_{FS} plots. Zero communication between J74 and injector J39-69I confirms that the section of the fault between these well-pair is sealing, extending from the section between two producers (J37–67P and J37-65) left of the fault and injector J39-69I. Similar to the well-pair of J37–65 and J40-64I, the zero communication between

J74 and injector J40-64I is likely due to limited sand facie continuity and other well-pair interactions. There is no communication between J74 and injector J41-67I, confirming that the section of the fault near J41-67I is sealing. There is significant communication between J74 and injector J43-67I, meaning that part of Fault “B” near J43-67I might be partially sealing. Strong connectivity exists between J74 and injector XS95I, combined with very high τ_{ij} . This well-pair therefore has impaired communication (see Fig. 31), meaning that this “strong connectivity” is questionable.

17.1.3. Producer J39-67

There is negligible connectivity between J39-67 and injector J37-67I, both left of Fault “B”. The sealing section of the fault extends up to just right of J39-67, resulting in zero connectivity between J39-67 and injector J39-69I. Zero connectivity between J39-67 and injector J40-64I is likely due to other well-pair interactions, especially between producer J39–65 and J40-64I. Zero communication between J39-67 and injector J41-67I confirms the sealing section of the fault near J41-67I. Several sealing sections of the fault, as well as other well-pair interactions led to no communication between J39-67 and two injectors: J43-67I and XS95I. Again, the dFC and I_{FS} plots depicted the single well-pair having non-zero λ_{ij} as having equal flow capacity per storage capacity.

17.1.4. Producer J40-70

There is negligible connectivity between J40-70 and injector J37-67I. This therefore means that a section of the fault near well J38-66 is likely partially sealing. Despite sand facie continuity in several layers and facie thickness greater than 2 m in most of these layers, there is no communication between J40-70 and injector J39-69I, both right of Fault “B”. Being active during similar periods in history (see Fig. 15), howbeit some differences in perforation intervals (see Fig. 17), it is evident that J39-69I did not influence any of the selected producers. Zero communication between J40-70 and injector J40-64I is likely due to several sealing sections along Fault “B” as well as interactions of other well-pairs. The negligible connectivity between J40-70 and injector J41-67I is a false positive, since $\tau_{ij} = 0.04$ month (about 1 day). This deduction is confirmed by the appearance of well-pair communication via infinite conductivity fractures as depicted by the dFC and I_{FS} plots (Figs. 30 and 31). There is negligible connectivity and consequently, impaired communication between J40-70 and injector J43-67I, both right of the fault. This is likely due to other interwell interactions and the relative distance of the well-pair. Zero connectivity and communication between J40-70 and injector XS95I is due several sealing sections of

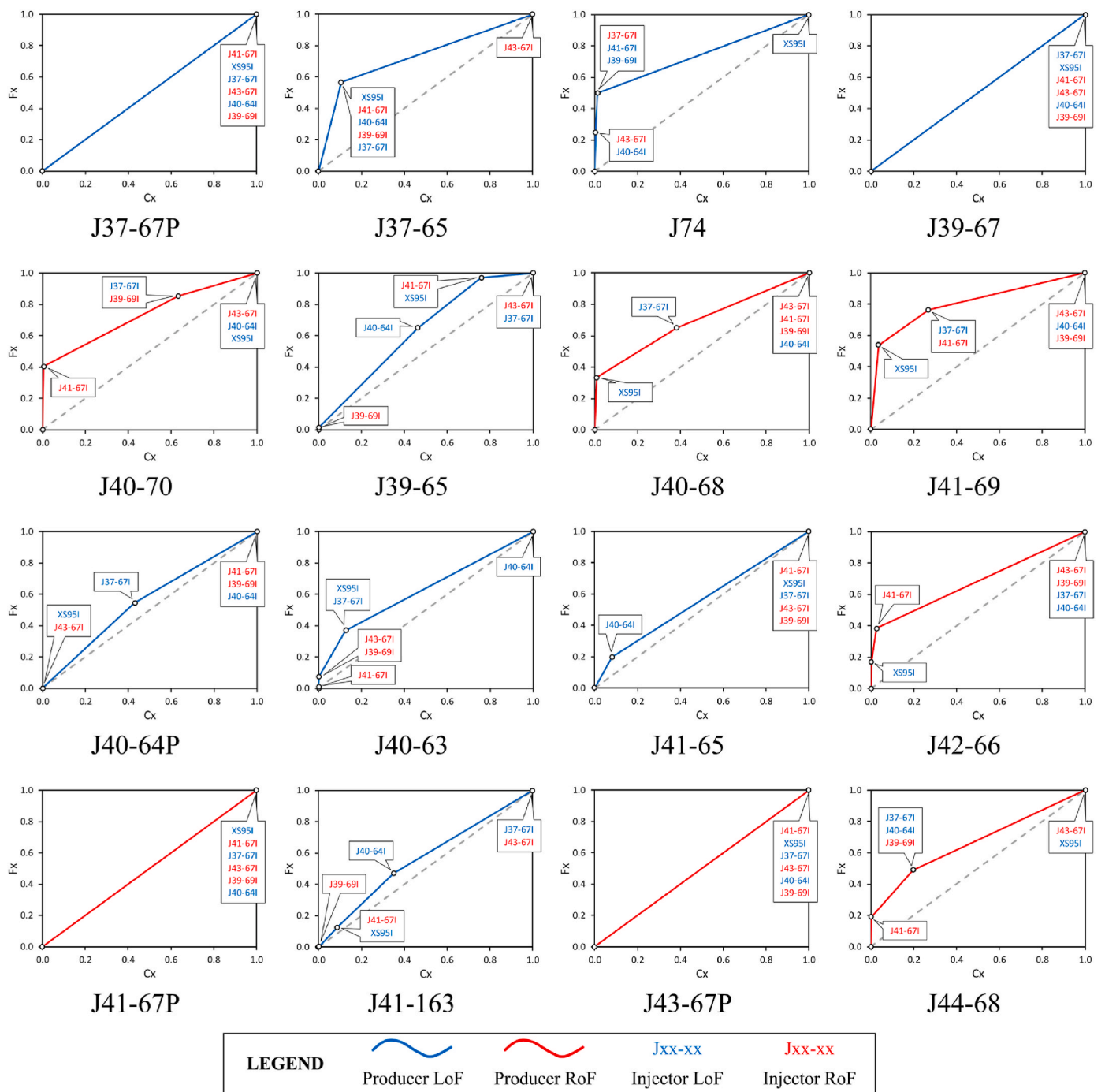


Fig. 30. Dynamic Flow Capacity (dFC) Plots of selected producers and injectors around Fault “B” in FEOF.

Fault “B” and other well-pair interactions.

17.1.5. Producer J39-65

There is no communication between J39-65 and injector J37-67I, both left of Fault “B”. This is likely due to other well-pair interactions. The insignificant connectivity between J39-65 and injector J39-69I, which is depicted as near-zero flow capacity per storage capacity and communication via highly conductive flow paths in the dFC and I_{FS} plots respectively, is a false positive since, $\tau_{ij} = 0.09$ month (about 2.5 days). There is significant communication between J39-65 and injector J40-64I, both left of Fault “B”, due to sand facie continuity in few layers

and similarities in perforation intervals. The negligible and insignificant connectivities between J39-65 and injectors J41-67I and J43-67I respectively, which as both right of the fault, confirms that the section of the fault near J41-67I is partially sealing. The zero connectivity between J39-65 and injector XS95I is likely due to two factors: (i.) other well-pair interactions; and (ii.) the section of Fault “B” near XS95I is likely sealing.

17.1.6. Producer J40-68

The negligible connectivity between J40-68 and injector J37-67I confirms that the section of Fault “B” near J37-67I is partially sealing.

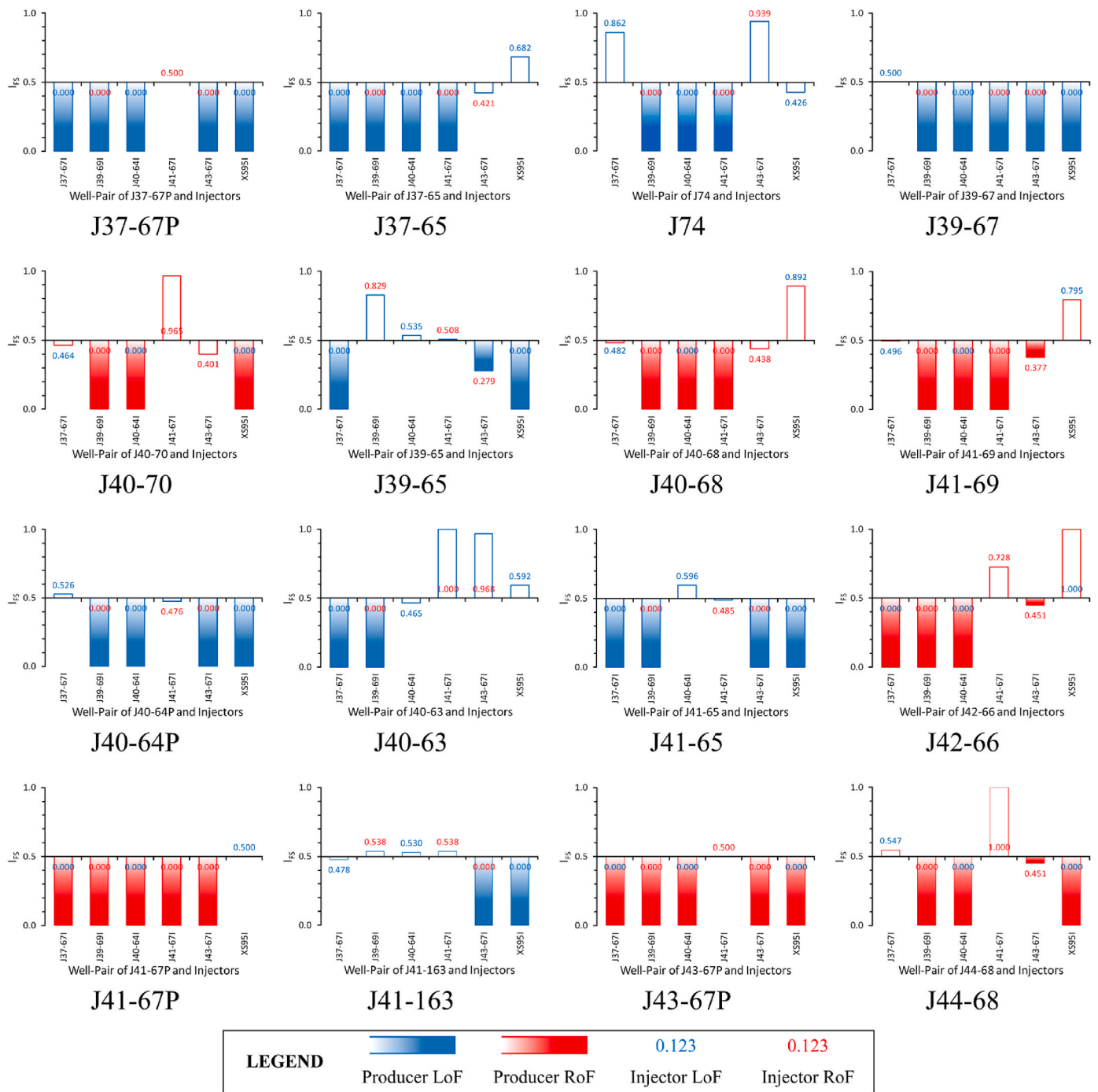


Fig. 31. Flow Storage Index (I_{FS}) Plots of selected producers and injectors around Fault “B” in FEOF.

Zero communication between J40-68 and injector J39-69I is likely due to limited sand facie continuity (see Fig. 7) with substantial thickness variations (see Fig. 8). Zero connectivity between J40-68 and injector J40-64I confirms that the section of the fault near J39-65 is sealing. In spite of sand facie continuity in nearly half of the layers, and facie thickness of up to 5.5 m between the well-pair, there is no communication between J40-68 and injector J41-67I. This is likely due to other well-pair interactions, such as between producer J42-66 and injector J41-67I. Due to other well-pair interactions, there is negligible connectivity and impaired communication ($I_{FS} = 0.438$) between J40-68 and injector J43-67I, both right of the fault. The negligible connectivity between J40-68 and injector XS95I, which is depicted as communication via infinite conductivity fractures (see Fig. 31), is likely a false positive since $\tau_{ij} = 0.11$ month (about 3 days).

17.1.7. Producer J41-69

The insignificant connectivity between J41-69 and injector J37-67I confirms that the section of Fault “B” near J37-67 is partially sealing. There is zero connectivity between J41-69 and J39-69I. Zero connectivity between J41-69 and injector J40-64I is likely due to other well-pair interactions, and limited sand facie continuity between the well-pair. Other well-pair interactions and substantial sand facie thickness variations led to zero connectivity between J41-69 and injector J41-67I, both right of Fault “B”, despite sand facie continuity in several layers. Insignificant connectivity and impaired communication between J41-69 and injector J43-67I is likely due to other well-pair interactions. Negligible connectivity between J41-69 and injector XS95I, which is depicted as communication via high conductivity fractures in dFC and I_{FS} plots, is likely a false positive.

17.1.8. Producer J40–64P

Other well-pair interactions likely led to negligible communication between J40–64P and injector J37–67I. Zero communication between J40–64P and injector J39–69I confirms the sealing section of Fault “B” near J39–67. The zero connectivity between J40–64P and J40–64I is expected since both wells represent the same well operated as producer and injector respectively. Negligible connectivity between J40–64P and injector J41–67I confirms that the section of Fault “B” near J41–67 is partially sealing. Communication between J40–64P and J37–67I well-pair and J40–64P and J41–67I well-pair are somewhat similar, resulting in fairly normal communication between these well-pairs ($I_{FS} \approx 0.5$), as shown in the I_{FS} plot. Zero connectivity and communication between J40–64P and J43–67I well-pair, as well as J40–64P and XS95I well-pair confirm that the sections of Fault “B” near these injectors are sealing.

17.1.9. Producer J40–63

There is no communication between J40–63 and injector J37–67I both left of the fault, likely due to interference from other well-pairs in between. With essentially no sand facie continuity and possible sealing sections of Fault “B” between J40–63 and injector J39–69I, there is zero connectivity and communication. The well-pair of J40–63 and injector J40–64I has a combination of strong connectivity and very high τ_{ij} , which makes the “strong connectivity” questionable. The insignificant connectivity between connectivity between J40–63 and injector J41–67I is likely a false positive since $\tau_{ij} = 0.05$ month (about 1.5 days). There is negligible connectivity between J40–63 and injector J43–67I, which is depicted as communication via infinite conductivity fractures in dFC and I_{FS} plots. Consequently, this “negligible connectivity” is questionable. In spite of the good communication between J40–63 and XS95I as depicted in the I_{FS} plot, a combination of strong connectivity ($\lambda_{ij} > 0.2$) with high τ_{ij} makes this “good communication” somewhat questionable.

17.1.10. Producer J41–65

Interactions between other wells and relative distance of the well-pair likely led to the zero connectivity between J41–65 and injector J37–67I. The zero connectivity between J41–65 and injector J39–69I confirms the sealing sections of Fault “B” in between this well-pair. There is insignificant connectivity between J41–65 and injector J40–64I, represented at improved communication in dFC and I_{FS} plots. The negligible connectivity between J41–65 and injector J41–67I confirms that the section of Fault “B” near J41–67 is partially sealing. In spite of the reported connectivities between J41–65 and these two injectors (J40–64I and J41–67I), the I_{FS} plot also depicts the effect of relative distance of these wells on their communication. Lack of connectivity and communication between J41–65 and injector J43–67I confirms that the section of the fault near J42–66 extending southwards is sealing. Zero connectivity between J41–65 and XS95I confirms that the section of the fault near XS95I is sealing.

17.1.11. Producer J42–66

The zero connectivity between J42–66 and injector J37–67P is likely due to several sealing sections of Fault “B” as well as other well-pair interactions. There is also zero connectivity between J42–66 and injector J39–69I, likely due to other well-pair interactions. Zero communication between J42–66 and injector J40–64I confirms that the section of Fault “B” near J42–66 is sealing. Significant connectivity and high communication exist between J42–66 and injector J41–67I between this well-pair (see Figs. 29 and 31 respectively). Although there appears to be strong connectivity between J42–66 and injector J43–67I, the I_{FS} plot depicts this as impaired communication, meaning that this strong connectivity is likely questionable. Considering the negligible connectivity between J42–66 and injector XS95I, combined with $\tau_{ij} = 0.04$ month and the portrayal of communication via infinite conductivity fractures in dFC and I_{FS} plots, the apparent communication of this well-pair is a false positive.

17.1.12. Producer J41–67P

With the exception of XS95I, there is zero connectivity between J41–67P and other selected injectors on both sides of the fault. A close look at the Activity Plot (see Fig. 15b) reveals that J41–67P was not active when these other selected injectors were active, leading to these zero connectivities. The zero connectivity between J41–67P and J41–67I is expected since both wells represent the same well operated as producer and injector respectively. There is insignificant connectivity between J41–67P and injector XS95I. However, this is likely a false positive since $\tau_{ij} = 0.11$ month. The depictions of “normal communication” between this well-pair using the dFC and I_{FS} plots are because, this is the only non-zero λ_{ij} well-pair for J41–65.

17.1.13. Producer J41–163

The strong connectivity (Fig. 29) and impaired communication (Fig. 31) between J41–163 and injector J37–67I, despite limited sand facie continuity between the wells (Fig. 7), the large relative distance of the well-pair (Fig. 11), interference from other well-pair interactions, and the relatively high τ_{ij} for that connectivity index, is questionable. Despite the depiction of “normal” communication between J41–163 and injector J39–69I (Fig. 31), the insignificant connectivity between this well-pair (Fig. 29a) is actually no connection (Fig. 30) because, both wells were active at different periods in history (Fig. 15b). There is strong connectivity between J41–163 and injector J40–64I, both left of the fault. The negligible connectivity between J41–163 and injector J41–67I confirms the partially sealing section of Fault “B” near J41–67. Zero connectivity between J41–163 and injector J43–67I confirms that the section of the fault in between this well-pair is sealing, extending from the section near J42–66. There is no communication between J41–163 and injector XS95I, both left of the fault.

17.1.14. Producer J43–67P

Zero connectivity between J43–67P and injector J37–67I is likely due to other well-pair interactions and several sealing sections of Fault “B”. There is zero connectivity between J43–67P and two injectors: J39–69I and J40–64I. On examining the Activity Plot (see Fig. 15b), J43–67P was not active during the periods J39–69I and J40–64I were active, leading to no communication between these wells. There is significant connectivity between J43–67P and injector J41–67I. Since this is the only non-zero λ_{ij} well-pair for J43–67P, the dFC and I_{FS} plots depict this as “normal communication” ($I_{FS} = 0.500$). Producer J43–67P and injector J43–67I represent well J43–67 operated as producer and injector respectively and therefore, the zero connectivity between them is expected. Zero connectivity between J43–67P and injector XS95I confirms that the section near XS95 is sealing.

17.1.15. Producer J44–68

The negligible connectivity between J44–68 and injector J37–67I confirms that the section of Fault “B” near J37–67I is partially sealing. The well-pair of J44–68 and J39–69I has zero connectivity, likely due to almost no sand facie continuity between the well-pair and other well-pair interactions. Zero connectivity between J44–68 and injector J40–64I confirms that the section of Fault “B” near J42–66 is sealing. The negligible connectivity between J44–68 and injector J41–67I, which is depicted as communication via infinite conductivity fractures in the dFC and I_{FS} plots, is a false positive since $\tau_{ij} = 0.05$ month (about 1.5 days). There is significant connectivity and slightly impaired communication ($I_{FS} = 0.451$) between J44–68 and J43–67I, both right of the fault. Zero connectivity between J44–68 and injector XS95I confirms that the section of Fault “B” near XS95I is sealing.

18. Discussion

Unlike the Dynamic Flow Capacity (dFC) plots, the Flow Storage Index (I_{FS}) plot presented in this study, is a new diagnostic plot used to capture and infer interwell communications in a reservoir of interest,

was applied to fault characterization of a real reservoir.

A diagnostic plot (the Flow Storage Index plot) and an iterative workflow were developed and validated using three synfield cases. Thereafter, optimized CRM parameters were combined with diagnostic (I_{FS}) plots, geological and well data to effectively characterize two selected faults and identify other flow barriers in a Far East Oil Field (FEOF). Based on the results, one fault had several sections with varying degrees of communication, and one sealing baffle on either side of the fault. The second selected fault was mostly sealing with no sealing baffles identified around the fault.

The Flow Storage Index (I_{FS}) plot addressed the limitations of the Dynamic Flow Capacity (dFC) plots. Although the CRM did not perfectly estimate production rates in the real field, the I_{FS} plots were used to quality-check the interwell connectivities obtained from CRM, identifying false positives and questionable interwell connectivities, thereby substantially improving the characterization of the selected faults. The IFS plots can also display the selected well's "perspective" in relation to other selected wells in field. The workflow presented can accommodate more data sets if available, or fewer data sets than used in this study. It also resolves some inconsistencies in the Facies and Thickness maps, which can lead to erroneous interwell communication inferences.

Combined with other data sources, the CRM and Diagnostic Plots can

be used to corroborate the results of Interference Testing, Tracer Test and 4D Seismic, in detecting and characterizing faults, as well as a cost-effective reservoir management and characterization tool.

Credit author statement

Oscar Ogali: Conceptualization, Methodology, Software, Data curation, Writing – Original draft preparation Oyinkepreye Orodu: Conceptualization, Methodology, Formal analysis, Data curation, Writing - Review & Editing, Resources, Supervision.

Declaration of competing interest

The authors declare that they have no known competing financial interests or personal relationships that could have appeared to influence the work reported in this paper.

Acknowledgments

The authors appreciate the Liaohe Oilfield Company of China National Petroleum Corporation for providing all related data used for previous works and this current study.

NOMENCLATURE

$q(t)$	production rate at time t
$w(t)$	injection rate at time t
P_{wf}	bottomhole flowing pressure (BHP)
t	time
J	productivity index
τ	time constant
c_t	total compressibility
V_p	pore volume
$\hat{q}(t)$	production rate at time t , estimated using CRM
$q(t_0)$	initial production rate, or production rate prior to analysis period
λ_{ij}	interwell connectivity index between injector-producer well-pair
N_i	total number of injectors interacting with a producer
I	total number of injectors
K	total number of producers
N	total number of time-steps
ν	interwell connectivity between producer-producer well-pair
$LB\tau$	lower bound of time constant
$UB\tau$	upper bound of time constant
R^2	coefficient of determination, or correlation coefficient
E_m	modified coefficient of efficiency
\bar{q}	mean of observed production rates, during the analysis period
$\hat{\bar{q}}$	mean of estimated production rates from CRM, during the analysis period
F	Flow Capacity
C	Storage Capacity
L_c	Lorenz Coefficient
V_{DP}	Dysktra-Parsons Coefficient
H_K	Koval Heterogeneity Factor
H'_K	Modified Koval Heterogeneity Factor
I_{FS}	Flow Storage Index

Subscripts and Superscripts

i	injector index
j	producer index
k	producer BHP index
m	number of the time-step
n	number of the current time-step
x	well-pair index

APPENDIX

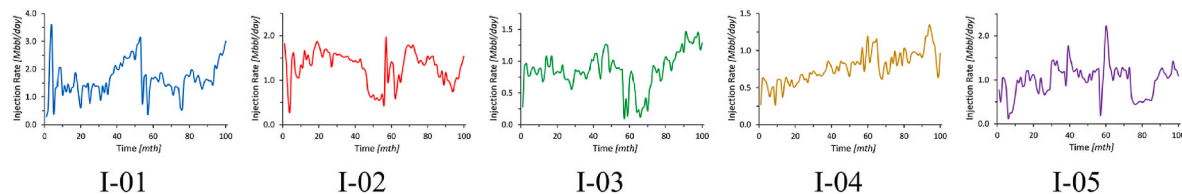


Fig. A1. Injection Rates of Injectors used in the Synfield Cases.

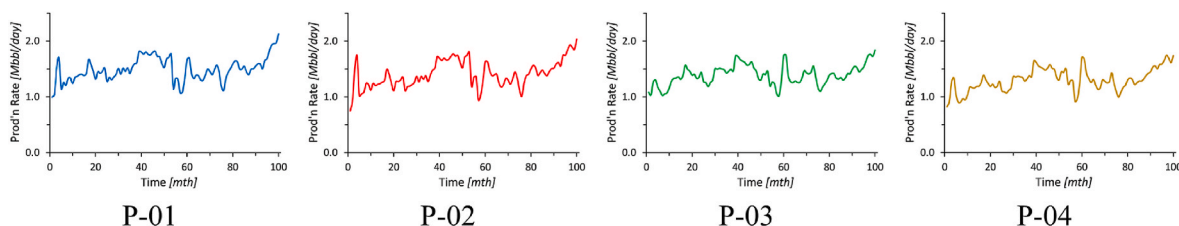


Fig. A2. Liquid Production Rates of Producers in Case A of the Synfield Cases.

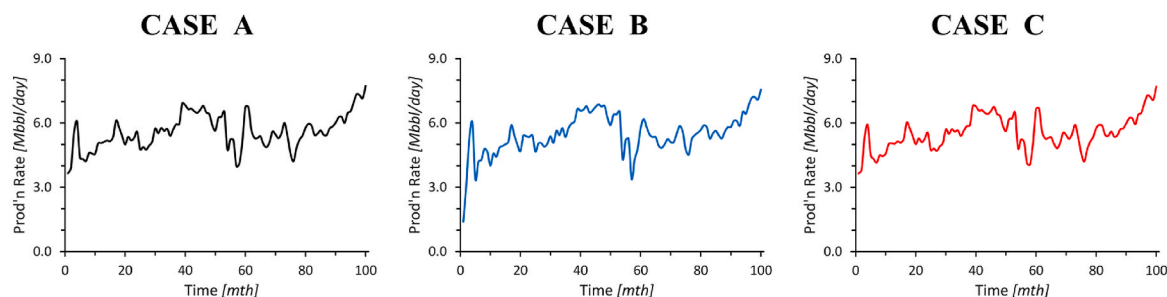


Fig. A3. Total Liquid Production Rates for the Synfield Cases.

References

- Al-Yousef, A.A., 2006. Investigating Statistical Techniques to Infer Interwell Connectivity from Production and Injection Rate Fluctuations. University of Texas at Austin.
- Albertoni, A., Lake, L.W., 2003. Inferring interwell connectivity only from well-rate fluctuations in waterfloods. *SPE Reservoir Eval. Eng.* 6 (1), 6–15. <https://doi.org/10.2118/83381-PA>.
- Altaheini, S., Al-Towjri, A., Ertekin, T., 2016. Introducing a New Capacitance-Resistance Model and Solutions to Current Modeling Limitations. Paper SPE-181311 Presented at 2016 SPE Annual Technical Conference and Exhibition. UAE, Dubai. <https://doi.org/10.2118/181311-MS>.
- Artun, E., 2016. Characterizing interwell connectivity in waterflooded reservoirs using data-driven and reduced-physics models: a comparative study. *Neural Comput. Appl.* 28 (7), 1729–1743. <https://doi.org/10.1007/s00521-015-2152-0>.
- Arunthavanathan, R., Khan, F., Ahmed, S., Imtiaz, S., 2021. A deep learning model for process fault prognosis. *Process Saf. Environ. Protect.* 154, 467–479. <https://doi.org/10.1016/j.psep.2021.08.022>.
- Aubert, I., Lamarche, J., Léonide, P., 2021. Ternary fault permeability diagram: an innovative way to estimate fault zones hydraulics. *J. Struct. Geol.* 147, 1–9. <https://doi.org/10.1016/j.jsg.2021.104349>.
- Batycky, R.P., Thiele, M.R., Baker, R.O., Chugh, S.H., 2008. Revisiting reservoir flood-surveillance methods using streamlines. *SPE Reservoir Eval. Eng.* 11 (2), 387–394. <https://doi.org/10.2118/95402-PA>.
- Biryukov, D., Kuchuk, F.J., 2012. Transient pressure behavior of reservoirs with discrete conductive faults and fractures. *Transport Porous Media* 95 (1), 239–268. <https://doi.org/10.1007/s11242-012-0041-x>.
- Cao, F., Luo, H., Lake, L.W., 2014. Development of a fully coupled two-phase flow based capacitance resistance model (CRM). *Proceedings - SPE Symposium on Improved Oil Recovery* 3, 1952–1967. <https://doi.org/10.2118/169485-MS>, 2002.
- Chen, H., Zhang, Z., Sun, W., Li, K., 2010. Modification of capacitance-resistive model for estimating waterflood performance. In: Paper SPE-99998 Presented at 2010 CPS/SPE International Oil and Gas Conference and Exhibition. <https://doi.org/10.2118/129783-MS>. Beijing, China.
- de Holanda, R.W., Gildin, E., Jensen, J.L., Lake, L.W., Kabir, S.C., 2018. A state-of-the-art literature Review on capacitance resistance models for reservoir characterization and performance forecasting. *Energies* 11 (12), 1–46. <https://doi.org/10.3390/en11123368>.
- Delshad, M., Bastami, A., Pourafshary, P., 2009. The use of capacitance-resistive model for estimation of fracture distribution in the hydrocarbon reservoir. In: Paper SPE-126076 Presented at 2009 SPE Saudi Arabia Section Technical Symposium and Exhibition. <https://doi.org/10.2118/126076-MS>, 2005, AlKhobar, Saudi Arabia.
- Dinh, A., Tiab, D., 2008. Inferring interwell connectivity from well bottomhole-pressure fluctuations in waterfloods. *SPE Reservoir Eval. Eng.* 11 (5), 874–881. <https://doi.org/10.2118/106881-PA>.
- Dou, H., 1995. Technologies used in the production of high pour point crude oil in shenyang oilfield. In: Paper SPE-29953 Presented at 1995 International Meeting on Petroleum Engineering. <https://doi.org/10.2118/29953-MS>. Beijing, China, 11–32.
- Ertekin, T., Abou-Kaseem, J.H., King, G.R., 2001. Introduction. In: Spivak, A., Killough, J.E. (Eds.), *Basic Applied Reservoir Simulation*, first ed. Society of Petroleum Engineers (SPE), pp. 1–21.
- Eshraghi, S.E., Rasaei, M.R., Zendejboudi, S., 2016. Optimization of miscible CO₂ EOR and storage using heuristic methods combined with capacitance/resistance and gentil fractional flow models. *J. Nat. Gas Sci. Eng.* 32, 304–318. <https://doi.org/10.1016/j.jngse.2016.04.012>.
- Fanchi, J.R., 2010. Porosity and permeability. In: *Integrated Reservoir Asset Management*, first ed. Gulf Professional Publishing, pp. 49–69. <https://doi.org/10.1016/b978-0-12-382088-4.00004-9>.
- Gherabati, S.A., Hughes, R.G., White, C.D., Zhang, H., 2017. A large scale network model to obtain interwell formation characteristics. *Int. J. Oil Gas Coal Technol.* 15 (1), 1–24. <https://doi.org/10.1504/IJOGCT.2017.083856>.
- Heffer, K.J., Fox, R.J., McGill, C.A., Koutsabeloulis, N.C., 1997. Novel techniques show links between reservoir flow directionality, earth stress, fault structure and geomchanical changes in mature waterfloods. *SPE J.* 2 (2), 91–98. <https://doi.org/10.2118/30711-PA>.
- Hosseini, S.A., 2019. Fault leakage detection and characterization using pressure transient analysis. *J. Petrol. Sci. Eng.* 176, 880–886. <https://doi.org/10.1016/j.petrol.2019.01.099>.
- Izgec, O., 2012. Understanding waterflood performance with modern analytical techniques. *J. Petrol. Sci. Eng.* 81, 100–111. <https://doi.org/10.1016/j.petrol.2011.11.007>.
- Izgec, O., Kabir, C.S., 2010. Quantifying Nonuniform Aquifer Strength at Individual Wells. *SPE Reservoir Evaluation and Engineering*, pp. 296–305. <https://doi.org/10.2118/120850-PA>. April 2010.

- Izgec, O., Kabir, C.S., 2012. Quantifying reservoir connectivity, in-place volumes, and drainage-area pressures during primary depletion. *J. Petrol. Sci. Eng.* 81, 7–17. <https://doi.org/10.1016/j.petrol.2011.12.015>.
- Jafroodi, N., Zhang, D., 2011. New method for reservoir characterization and optimization using CRM-EnOpt approach. *J. Petrol. Sci. Eng.* 77 (2), 155–171. <https://doi.org/10.1016/j.petrol.2011.02.011>.
- Jansen, F.E., Kelkar, M.G., 1997. Application of wavelets to production data in describing inter-well relationships. In: Paper SPE-38876 Presented at 1997 SPE Annual Technical Conference and Exhibition, pp. 323–330. <https://doi.org/10.2118/38876-MS>. San Antonio, Texas.
- Jensen, J.L., Lake, L.W., Corbett, P.W.M., Goggin, D.J., 1997. *Statistics for Petroleum Engineers and Geoscientists*. Prentice Hall Inc.
- Kaviani, D., Jensen, J.L., Lake, L.W., 2012. Estimation of interwell connectivity in the case of unmeasured fluctuating bottomhole pressures. *J. Petrol. Sci. Eng.* 90 (91), 79–95. <https://doi.org/10.1016/j.petrol.2012.04.008>.
- Kaviani, D., Soroush, M., Jensen, J.L., 2014. How accurate are capacitance model connectivity estimates? *J. Petrol. Sci. Eng.* 122, 439–452. <https://doi.org/10.1016/j.petrol.2014.08.003>.
- Kaviani, D., Valkó, P.P., 2010. Inferring interwell connectivity using multiwell productivity index (MPI). *J. Petrol. Sci. Eng.* 73, 48–58. <https://doi.org/10.1016/j.petrol.2010.05.006>.
- Keranan, K.M., Savage, H.M., Abers, G.A., Cochran, E.S., 2013. Potentially induced earthquakes in Oklahoma, USA: links between wastewater injection and the 2011 Mw 5.7 earthquake sequence. *Geology* 41 (6), 699–702. <https://doi.org/10.1130/G34045.1>.
- Koval, E.J., 1963. A method for predicting the performance of unstable miscible displacement in heterogeneous media. *Soc. Petrol. Eng. J.* 3 (2), 145–154. <https://doi.org/10.2118/450-PA>.
- Lake, L.W., 1989. *Volumetric sweep efficiency*. In: *Enhanced Oil Recovery*. Prentice Hall Inc, pp. 188–233.
- Laochamnonvorapongse, R., Kabir, C.S., Lake, L.W., 2014. Performance assessment of miscible and immiscible water-alternating gas floods with simple tools. *J. Petrol. Sci. Eng.* 122, 18–30. <https://doi.org/10.1016/j.petrol.2014.08.012>.
- Lee, K.-H., Ortega, A., Jafroodi, N., Ershaghi, I., 2010. A multivariate autoregressive model for characterizing producer-producer relationships in waterfloods from injection/production rate fluctuations. In: Paper SPE-132625 Presented at 2010 SPE Western Regional Meeting, vol. 1, pp. 451–461. <https://doi.org/10.2118/132625-MS>, 2008, Anaheim, California, U.S.A.
- Lee, K.-H., Ortega, A., Nejad, A.M., Jafroodi, N., Ershaghi, I., 2009. A novel method for mapping fractures and high permeability channels in waterfloods using injection and production rates. In: Paper SPE-121353 Presented at 2009 SPE Western Regional Meeting. <https://doi.org/10.2118/121353-MS>. San Jose, California, U.S.A., 461–472.
- Legates, D.R., McCabe, G.J., 1999. Evaluating the use of “goodness-of-fit” measures in hydrologic and hydroclimatic model validation. *Water Resour. Res.* 35 (1), 233–241. <https://doi.org/10.1029/1998WR900018>.
- Lesan, A., Eshraghi, E.S., Bahroudi, A., Rasaei, R.M., Rahami, H., 2018. State-of-the-Art solution of capacitance resistance model by considering dynamic time constants as a realistic assumption. *Journal of Energy Resources Technology, Transactions of the ASME* 140 (1), 1–14. <https://doi.org/10.1115/1.4037368>.
- Liang, X., Weber, D.B., Edgar, T.F., Lake, L.W., Sayarpour, M., Al-Yousef, A., 2007. Optimization of oil production based on a capacitance model of production and injection rates. In: Paper SPE-107713 Presented at 2007 SPE Hydrocarbon Economics and Evaluation Symposium. <https://doi.org/10.2118/107713-MS>. Dallas Texas, USA.
- Liu, F., Mendel, J.M., Nejad, A.M., 2009. Forecasting injector/producer relationships from production and injection rates using an extended kaiman filter. *SPE J.* 14 (4), 653–664. <https://doi.org/10.2118/110520-PA>.
- Liu, K., Wu, X., Ling, K., 2019. Integrated detection of water production in a highly heterogeneous and tight formation using CRM model: a case study on water flooding gaiter draw unit, Wyoming, USA. In: *International Petroleum Technology Conference 2019*. <https://doi.org/10.2523/iptc-19333-MS>. IPTC 2019.
- Liu, Q., Lu, H., Li, L., Mu, A., 2018. Study on characteristics of well-test type curves for composite reservoir with Sealing faults. *Petroleum* 4 (3), 309–317. <https://doi.org/10.1016/j.petlm.2018.03.011>.
- Malik, Z.A., Silva, B.A., Brimhall, R.M., Wu, C.H., 1993. An integrated approach to characterize low-permeability reservoir connectivity for optimal waterflood infill drilling. In: Paper SPE-25853 Presented at 1993 SPE Rocky Mountain Regional/Low Permeability Reservoirs Symposium. <https://doi.org/10.2118/25853-MS>. Colorado, U.S.A., 119–128.
- Mamghaderi, A., Pourafshary, P., 2013. Water flooding performance prediction in layered reservoirs using improved capacitance-resistive model. *J. Petrol. Sci. Eng.* 108, 107–117. <https://doi.org/10.1016/j.petrol.2013.06.006>.
- Mohamaddally, M., Soroush, M., Zeidouni, M., Alexander, D., Boodlal, D., 2018. Fault leakage assessment using the capacitance model. In: Paper SPE-191250 Presented at 2018 SPE Trinidad and Tobago Section Energy Resources Conference, Port of Spain. <https://doi.org/10.2118/191250-MS>. Trinidad and Tobago.
- Moreno, G.A., 2013. Multilayer capacitance – resistance model with dynamic connectivities. *J. Petrol. Sci. Eng.* 109, 298–307. <https://doi.org/10.1016/j.petrol.2013.08.009>.
- Moretti, I., 1998. The role of faults in hydrocarbon migration. *Petrol. Geosci.* 4 (1), 81–94. <https://doi.org/10.1144/petgeo.4.1.81>.
- Mosaheb, M., Zeidouni, M., 2018. Above zone pressure interpretation for leaky well characterization and its identification from leaky caprock/fault. *J. Petrol. Sci. Eng.* 171 (July), 218–228. <https://doi.org/10.1016/j.petrol.2018.07.035>.
- Nguyen, A.P., Kim, J.S., Lake, L.W., Edgar, T.F., Haynes, B., 2011. Integrated capacitance resistive model for reservoir characterization in primary and secondary recovery. In: Paper SPE-147344 Presented at 2011 SPE Annual Technical Conference and Exhibition. <https://doi.org/10.2118/147344-MS>. Denver, Colorado, USA.
- Ogali, O.I.O., Orodu, O.D., 2020. Flow barrier detection and characterisation using capacitance-resistance model: case study of a Far East oil field. In: Paper SPE-203735 Prepared for 2020 SPE Nigerian Annual International Conference and Exhibition. <https://doi.org/10.2118/203735-MS>. Lagos, Nigeria.
- Oliveira, D.S., Horowitz, B., Tueros, J.A.R., 2021. Ensemble-based method with combined fractional flow model for waterflooding optimization. *Oil Gas Sci. Technol.* 76 (7), 1–16. <https://doi.org/10.2516/ogst/2020090>.
- Orodu, Orinkepreye David, 2009. *Reservoir Characterization, Simulation and Optimization: High Paraffinic Oil Content Reservoir, Block Shen-95, Liaohu Oilfield*. China University of Geosciences, North-East China.
- Orodu, Oyinkepreye D., Tang, Z., Nwonodi, C., 2008. Reservoir paraffin precipitation influence: south fault-block of block shen-95 , liaohe oilfield. In: North-East China. Paper SPE-119728 Presented at 2008 SPE Annual International Technical Conference and Exhibition, Abuja, Nigeria, pp. 1–18. <https://doi.org/10.2118/119728-MS>.
- Panda, M.N., Chopra, A.K., 1998. An integrated approach to estimate well interactions. In: Paper SPE-39563 Presented at 1998 SPE India Oil and Gas Conference and Exhibition, pp. 517–530. <https://doi.org/10.2118/39563-MS>. New Delhi, India.
- Pouladi, B., Sharifi, M., Akbari, M.R., Hosseini-Nasab, S.M., 2018. A new numerical well testing approach: application to characterization of complex fault structures. *Petroleum* 5 (3), 295–302. <https://doi.org/10.1016/j.petlm.2018.07.001>.
- Rutqvist, J., Birkholzer, J., Cappa, F., Tsang, C.-F., 2007. Estimating maximum sustainable injection pressure during geological sequestration of CO2 using coupled fluid flow and geomechanical fault-slip analysis. *Energy Convers. Manag.* 48 (6), 1798–1807. <https://doi.org/10.1016/j.enconman.2007.01.021>.
- Salazar, M., Gonzalez, H., Matringe, S., Castiñeira, D., 2012. Combining decline-curve analysis and capacitance-resistance models to understand and predict the behavior of a mature naturally fractured carbonate reservoir under gas injection. In: Paper SPE-153252 Presented at 2012 SPE Latin American and Caribbean Petroleum Engineering Conference. <https://doi.org/10.2118/153252-MS>. Mexico City, Mexico.
- Sayarpour, M., Zuluaga, E., Kabir, C.S., Lake, L.W., 2009. The use of capacitance-resistance models for rapid estimation of waterflood performance and optimization. *J. Petrol. Sci. Eng.* 69 (3–4), 227–238. <https://doi.org/10.1016/j.petrol.2009.09.006>.
- Sayyafzadeh, M., Pourafshary, P., Haghghi, M., Rashidi, F., 2011. Application of transfer functions to model water injection in hydrocarbon reservoir. *J. Petrol. Sci. Eng.* 78 (1), 139–148. <https://doi.org/10.1016/j.petrol.2011.05.009>.
- Shahvali, M., Shirzadi, S.G., Ballin, P.R., Ziegel, E., 2012. Waterflood management based on well Allocation factors for improved sweep efficiency: model based or data based?. In: Paper SPE-153912 Presented at 2012 SPE Western Regional Meeting. <https://doi.org/10.2118/153912-MS>. Bakersfield, California, U.S.A., 747–753.
- Soerawinata, T., Kelkar, M.G., 1999. Reservoir management using production data. In: Paper SPE-52224 Presented at 1999 SPE Mid-continent Operation Symposium. <https://doi.org/10.2118/52224-MS>. Oklahoma, U.S.A.
- Soroush, M., Kaviani, D., Jensen, J.L., 2014. Interwell connectivity evaluation in cases of changing skin and frequent production interruptions. *J. Petrol. Sci. Eng.* 122, 616–630. <https://doi.org/10.1016/j.petrol.2014.09.001>.
- Soroush, M., Rasaei, M.R., 2018. Application of the capacitance model in primary production period before IOR implementation. In: Paper SPE-191236 Presented at 2018 SPE Trinidad and Tobago Section Energy Resources Conference, Port of Spain, Trinidad and Tobago. <https://doi.org/10.2118/191236-MS>.
- Takam Takougang, E.M., Ali, M.Y., Bouzidi, Y., Bouchaala, F., Sultan, A.A., Mohamed, A. I., 2019. Extraction and characterization of faults and fractures from 3D VSP data in a carbonate reservoir: a workflow. *J. Petrol. Sci. Eng.* 182, 1–12. <https://doi.org/10.1016/j.petrol.2019.106328>.
- Thiele, M.R., Batycky, R.P., Fenwick, D.H., 2010. Streamline simulation for modern reservoir-engineering workflows. *J. Petrol. Technol.* 62 (1), 64–70. <https://doi.org/10.2118/118608-MS>.
- Thiele, Marco R., Batycky, R.P., 2003. *Water injection optimization using a streamline-based workflow*. In: Paper SPE-84080 Presented at 2003 SPE Annual Technical Conference and Exhibition, Denver, Colorado, U.S.A. <http://doi.org/https://doi.org/10.2118/84080-MS>.
- Wang, H., Han, J., Zhang, K., Yao, C., Ma, X., Zhang, L., Yang, Y., Zhang, H., Yao, J., 2021. An interpretable interflow simulated graph neural network for reservoir connectivity analysis. *SPE J.* 26 (4), 1636–1651. <https://doi.org/10.2118/205024-PA>.
- Weber, D., Edgar, T.F., Lake, L.W., Lasdon, L., Kawas, S., Sayarpour, M., 2009. Improvements in capacitance-resistive modeling and optimization of large scale reservoirs. *Paper SPE-121299 Presented at 2009 SPE Western Regional Meeting, California*, 1–17. <https://doi.org/10.2118/121299-MS>.
- Wu, X., Hale, D., 2016. 3D seismic image processing for faults. *Geophysics* 81 (2), IM1–IM11. <https://doi.org/10.1190/GEO2015-0380.1>.
- Yaxley, L.M., 1987. Effect of a Partially Communicating Fault on Transient Pressure Behavior. *SPE Formation Evaluation*, pp. 590–598. <https://doi.org/10.2118/14311-PA>.
- Yousef, A.A., Lake, L.W., Jensen, J.L., 2006. Analysis and interpretation of interwell connectivity from production and injection rate fluctuations using a capacitance model. In: Paper SPE-99998 Presented at 2006 SPE/DOE Symposium on Improved Oil Recovery. <https://doi.org/10.2118/99998-MS>. Tulsa, Oklahoma, USA.
- Yousef, Ali A., Gentil, P., Jensen, J.L., Lake, L.W., 2005. A capacitance model to infer interwell connectivity from production- and injection-rate fluctuations. *SPE Reservoir Eval. Eng.* 9 (6), 630–646. <https://doi.org/10.2118/95322-PA>.

Yousefi, S.H., Rashidi, F., Sharifi, M., Soroush, M., 2019. Prediction of immiscible gas flooding performance: a modified capacitance–resistance model and sensitivity analysis. *Petrol. Sci.* 16 (5), 1086–1104. <https://doi.org/10.1007/s12182-019-0342-6>.

Yu, J., Jahandideh, A., Hakim-Elahi, S., Jafarpour, B., 2021. Sparse neural networks for inference of interwell connectivity and production prediction. *SPE J.* 1–22 <https://doi.org/10.2118/205498-PA>.

Zhang, L., Luo, X., Vasseur, G., Yu, C., Yang, W., Lei, Y., Song, C., Yu, L., Yan, J., 2011. Evaluation of geological factors in characterizing Fault connectivity during hydrocarbon migration: application to the bohai bay basin. *Mar. Petrol. Geol.* 28 (9), 1634–1647. <https://doi.org/10.1016/j.marpetgeo.2011.06.008>.